A computational framework for low-cycle fatigue in polycrystalline materials

Article *in* Computer Methods in Applied Mechanics and Engineering · May 2021

DOI: 10.1016/j.cma.2021.113898

CITATIONS
6

READS
103

3 authors:

Francesco Parrinello
Università degli Studi di Palermo
43 PUBLICATIONS **484** CITATIONS
SEE PROFILE

Vincenzo Gulizzi
Università degli Studi di Palermo
58 PUBLICATIONS **528** CITATIONS
SEE PROFILE

Ivano Benedetti
Università degli Studi di Palermo
127 PUBLICATIONS **1,337** CITATIONS
SEE PROFILE

A computational framework for low-cycle fatigue in polycrystalline materials

Francesco Parrinello[a], Vincenzo Gulizzi[b], Ivano Benedetti[a,*]

[a] *Department of Engineering, University of Palermo, Viale delle Scienze, Edificio 8, Palermo, 90128, Italy*
[b] *Center for Computational Sciences and Engineering (CCSE), Lawrence Berkeley National Laboratory MS 50A-3111, Berkeley, CA 94720, USA*

Abstract

A three-dimensional framework for low-cycle fatigue analysis of polycrystalline aggregates is proposed in this work. First, a cohesive law coupling plasticity and damage is developed for modelling cycle-by-cycle degradation of material interfaces up to complete de-cohesion and failure. The law may model both quasi-static degradation under increasing monotonic load and degradation under cyclic loading, through a coupled plasticity-damage model whose activation and flow rules are formulated in a thermodynamically consistent framework. The proposed interface laws have been then implemented and coupled with a multi-region boundary element formulation, with the aim of analysing low-cycle intergranular fatigue in polycrystalline aggregates. The boundary element formulation allows expressing the micro-mechanical problem in terms of grain-boundary displacements and tractions only, which are the quantities directly entering the cohesive laws, thus simplifying the coupling of the two tools. After assessing the response of an individual interface, to both quasi-static and cyclic loads, the coupled framework has been employed for the computational investigation of low-cycle degradation in fully-3D and pseudo-3D, or 2D columnar, polycrystalline aggregates, assuming that the degradation process remains confined in the intergranular regions. The discussed results show the potential of the developed formulation for *multiscale materials modelling*, which may find future application in the multiscale design of engineering structures subjected to complex loads and degradation processes, and for *computational micromechanics*, which may find direct application in the design and analysis of micro-electromechanical systems (MEMS).

Keywords: Polycrystalline materials, Low-cycle fatigue, Cohesive Zone Modelling, Multiscale

*Corresponding author
Email address: ivano.benedetti@unipa.it (Ivano Benedetti)

1. Introduction

In the last decades, several fields of science and engineering have witnessed an increased interest towards the understanding and manipulation of *materials microstructures*. Such interest and the accompanying increase in the number of studies devoted to materials micro-/multi-scale mechanics have different reasons and aims [1].

On one hand, besides the purely scientific and inquisitive interest, the need of manufacturing structures presenting a balance of often contrasting properties, such as stiffness, strength, toughness, low weight, has motivated industrial and academic communities to investigate about and focus on the complex interactions between the mechanical component level, where the operational conditions are specified, and the materials microstructure, with the ambitious aim of developing materials with features *tailored* on the specific application. An example in this sense is provided by the remarkable development of fibre reinforced composites in the aerospace industry, in which the width and versatility of the material design space, provided e.g. by the variety of possible matrix-fibres arrangements, offers a broad array of choices for manufacturing components whose properties are optimised along selected load paths, consider e.g. the recent emergence of variable angle tow composites [2].

On the other hand, the rapid developments in miniaturisation and the widespread employment of applications involving micro-electro-mechanical devices (MEMS) [3], either sensors, actuators or other kinds of transducers, in which the application scale is comparable with that of the materials basic constituents and the separation of scale cannot be *a-priori* assumed, has justified further research into micromechanics itself, irrespective of possible influence on materials properties at larger scales.

The study of materials micromechanics and of the link between materials microscopic features and structural performances is particularly challenging and intriguing when the issue of damage is considered. In such a framework, the analysis of the conditions under which damage initiates and evolves at the *micro*-scale and then coalesces and migrates to the *macro*-scale, where it may progress up to inducing component and structural failure, is of special interest [4]. The comprehension of such damage initiation and evolution mechanisms has direct technological significance and, at different maturity levels, is at the heart of modern design practices: while its role in the manufacturing

of MEMS may be immediately apparent, in the aerospace industry, for example, the application of fracture mechanics, which is the basis for the development of *damage tolerance* approaches to aircraft structural design and maintenance, could noticeably benefit from the development of enhanced microstructure-based understanding and simulation of crack initiation and propagation mechanisms.

In recent years, research on materials micromechanics has been boosted by the development of high-resolution experimental techniques for materials microstructural characterisation, see e.g. Ref.[5]. Such methodologies provide a wealth of information that may help elucidate the mechanisms underlying the development of damage in several classes of materials. However, relying on a complete experimental characterisation for the development of a new material, or the enhancement of an existing one, may attract remarkable costs, especially when the design space involves a high number of different choices. A more effective approach is based on the combined use of essential experimental information *and* computational models able to accommodate experimental data in a consistent representation of the material mechanics. Such combined approach has benefitted from the progress of *high performance computing* (HPC), which allows the inclusion and processing of ever increasing amounts of information provided by the refinement of the mentioned characterisation techniques.

In the above background, the present contribution is devoted to the development of a microstructural model for the analysis of degradation and cracking in polycrystalline materials under cyclic load, namely to low-cycle fatigue analysis. Polycrystalline materials, either metals, alloys or ceramics, are extensively employed in several fields of engineering. In a modelling perspective, their properties, behaviour and performances have beed investigated using either phenomenological approaches, which form the basis of traditional engineering practices, or more recent physically based approaches, attempting to understand how macroscopic properties emerge form the microstructural features.

In the case of polycrystalline materials, aggregate properties are induced by the inherent features of the individual grains (morphology, crystallographic nature and orientation, defects, etc.) and by the physical/chemical character of the intergranular interfaces, which identify discontinuity regions within the aggregate and are often the seat of damage initiation processes. Models investigating such materials in a multiscale perspective usually retain more or less refined representations of the aggregate morphology and its interfaces [6, 7, 8]. Starting from such morphological representations,

one of the most popular approaches to polycrystalline materials degradation and cracking is based on the employment of the finite element method (FEM) in conjunction with cohesive zone modelling (CZM) [9, 10, 11].

The present framework is based on a different approach and, instead of FEM, boundary integral equations are employed to model the mechanics of the individual grains. In detail, the framework is based on the following key items: *a*) a Laguerre-Voronoi representation of the aggregate morphologies, which allows to retain the main statistical features of real polycrystalline materials [12, 13]; *b*) a boundary integral model for the mechanics of individual grains, numerically addressed through the boundary element method (BEM) [14, 15]; *c*) an original and thermodynamically consistent cohesive law, able to represent the development and accumulation of intergranular damage under either static or cyclic loads, through a hysteretic damage-plasticity approach.

Previously, boundary element models have been developed for polycrystalline two-dimensional quasi-static or dynamic micro-cracking [16, 17, 18, 19], three-dimensional computational homogenisation and micro-cracking of common and piezoelectric aggregates [20, 21, 22, 23, 24, 25], stress corrosion cracking [26] and multiscale analysis of degradation and fracture [27, 28, 29]. In Ref.[30] a boundary integral formulation for high-cycle fatigue has been proposed: since the simulation of individual cycles would be unpractical or even unfeasible in high-cycle fatigue problems, typically featuring $N_c > 10^5$ cycles, especially when the material microstructure is explicitly represented, the formulation was based on a series of assumptions (damage decomposition and evolution rules) and strategies (envelope load and cycles jump) addressed at estimating, under some definite conditions, the development of damage over a large number of cycles without resorting to the accurate representation of mechanisms within individual cycles.

While such methods may help estimate the fatigue life of engineering components, in some classes of problems it may be useful to analyse how damage develops on a cycle-by-cycle basis [31, 32]. Example are provided in Ref.[33], where fatigue damage in pure polycrystalline magnesium under cyclic tension-compression loading is addressed, and in Refs.[34, 35], devoted to the analysis of fatigue degradation in polysilicon, a material often employed in MEMS, which present specific features and complexities, still open to investigation.

In the present work, an original cohesive law is first proposed for modelling intergranular degradation on a cycle-by-cycle basis; such law is subsequently integrated into a Laguerre-Voronoi multi-region boundary element framework for the analysis of intergranular degradation and cracking in

polycrystalline aggregates. A word of caution is necessary for defining the scope of the study and avoiding inappropriate extensions. Low-cycle fatigue cracking in polycrystalline materials is generally related to the interaction of several complex mechanisms [36] and no universal initiation mechanism is easily identifiable. The present study develops an approach that may be useful for the analysis of materials in which plasticity is highly restrained within the grains and mainly confined within the grain boundaries, as suggested for polysilicon e.g. in Ref.[34]. In more general cases, the present approach may be used in conjunction with other techniques or laws, in the attempt to capture more complex behaviours, see Section 6.

The outline of the paper is as follows. Section 2 discusses the generation of Laguerre-Voronoi tessellations as an artificial digital model of polycrystalline microstructures. Section 3 details the development of the proposed cohesive law, able to represent damage and plasticity accumulation under cyclic loading, and discusses its features. Section 4 describes the three-dimensional polycrystalline boundary element framework and discusses the integration of the developed cohesive laws. The set-up and results of the performed computational tests are reported in Section 5, while some general discussion follows in Section 6, before the *Conclusions*.

2. Virtual polycrystalline aggregates

To investigate the mechanics of polycrystalline aggregates, it is necessary to provide a suitable representation of their morphology. In this work, aggregates of grains with different crystallographic orientations in the three-dimensional space are considered and their morphology is generated through Voronoi-Laguerre tessellations [12, 6, 13]. Such tessellations are generated through mathematically well defined algorithms and provide space filling subdivisions of the analysis domain, which may represent suitable approximations of real polycrystalline microstructures, as discussed e.g. in Ref.[13].

From the operative point of view, given the generic analysis domain V bounded by the frontier ∂V, the tessellations can be effectively generated employing open source software packages such as `Voro++` (`http://math.lbl.gov/voro++/`) [37] or `Neper` (`https://neper.info/#`) [12]. In principle, with such tools, either *convex* or *non-convex* domains may be tessellated. However, non-convex domains, which might be useful to represent actual micro-devices (micro-beams, brackets, gears, etc.), may require a slightly more sophisticated employment of the tessellation algorithms and packages, see e.g. Refs.[38, 30]. From this point of view, it is interesting to mention that `Neper`

has recently been endowed with methods easing such task. Additionally, it is possible to generate *periodic non-prismatic* tessellations, in which no grain is trimmed by the walls of the bounding box ∂V defining the original volume V: such morphologies may be useful to remove boundary artefacts originating from mesh distortions introduced by cutting operations and mechanical boundary effects related to the presence of boundary grains of altered morphology. Such a kind of tessellations will not be used in the present contribution, as it has been assessed and discussed in Ref.[21], to which the interested readers are referred.

A remarkable feature of Laguerre-Voronoi tessellations is the fact that each cell g, associated with a specific crystal in the aggregate, is a convex polyhedron bounded by *flat* convex polygonal faces. As it will be described in Section 4, this aspect, in conjunction with the boundary integral nature of the proposed formulation, induces well defined and noticeable simplification in the discretisation and numerical integration procedures.

Fig.(1) illustrates some examples of tessellations that may be considered within the present framework. In general a generic grain is in contact with a set of neighbouring grains, with which it interacts through the shared interfaces. In the present work, the interaction between grains is modelled through cohesive laws able to represent the initiation and evolution of damage under the action of either quasi-static monotonic loads or cyclic loads, on a cycle-by-cycle approach. The formulation of such cohesive laws is described in next Section.

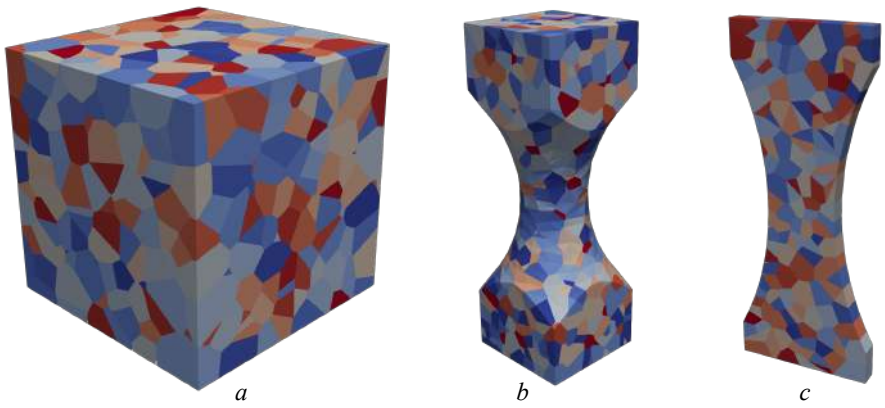

Figure 1: Different kinds of morphologies can be generated and analysed in the proposed framework: *a*) example of 1000-grain tessellation of a convex prismatic domain; *b*) fully-3D tessellation of a non-convex domain; *c*) example of pseudo-3D, or 2D columnar tessellation.

3. Low-cycle fatigue interface

The theoretical details about the proposed elastic-plastic cohesive-law with damage for interfaces subjected to the action of cyclic loads are given, after a brief introductory review of models available in the literature.

Cohesive Zone Modelling is now a well developed framework for the analysis de-cohesion and fracture phenomena. Different kinds of cohesive interface models with specific features have been proposed. Examples are provided by isotropic and orthotropic cohesive laws [39], cohesive laws coupling damage and plasticity [40], laws capturing different mode I and mode II fracture energies [41, 42, 43], thermodynamically consistent laws [44, 45, 46], laws focusing on the smooth transition from cohesive to frictional behaviour [47, 44] and laws able to represent finite displacement conditions [41, 48].

Several contributions have been specifically addressed at the analysis of interfaces subjected to the action of cyclic loads: in Ref.[31], stiffness degradation in the re-loading branch of the loading cycle is considered, but not developed in a damage framework; in Ref.[32] the CZM developed in Ref.[49] is modified in a form suitable for cyclic loading; in Ref.[50], damage is assumed to be a function of the accumulated plastic shear strain; a continuum damage mechanics approach to fatigue analysis is developed in Ref.[51], where the threshold damage is function of the cycle number; a plastic damage model is proposed in Ref.[52] for the analysis of ultra-low-cycle fatigue problems, where the damage is governed by a strain softening parameter that takes into account the amount of volumetric fracture energy dissipated by the material; a coupled damage-plasticity model for the analysis of cyclic behaviour of interfaces under shear loads is defined in Ref.[53], with damage evolution only at the unloading plastic process; the fatigue behaviour of brittle materials is modelled in Ref.[54], in a phase-field approach with a fatigue degradation as function of a cumulated history variable.

The above references represent a short summary of the interface models available in the literature. From this survey, it is realised that most of the available formulations for low-cycle fatigue analysis are not defined in a consistent thermodynamic framework: several cohesive laws are not based on a Helmholtz free energy function and the actual dissipation related to the cyclic material degradation cannot be neither defined nor evaluated. In most low-cycle fatigue formulations, cyclic degradation is not modelled by specific evolution laws, functions of the state variables in the loading cycle, but they are modelled resorting to Peerling-like laws [55], as function of the stress cycle

amplitude, the mean stress in the cycle and the number of loading cycles.

In this work, we propose novel thermodynamically consistent cohesive laws, based on a suitably defined Helmholtz free energy function, where the material behaviour is governed by a pointwise set of state variables (plastic deformation, damage, internal variables, etc.). Traction components, evolution of plastic and damage variables and the relevant constitutive equations are derived by following the classical Coleman and Noll procedure [56] and the model satisfies the second thermodynamic law by proving that dissipation is null for any elastic loading step and is non-negative for any loading path involving plastic or damage increments.

While the present section details the theoretical derivation, the computational use of the developed interface laws in conjunction with the polycrystalline boundary element framework is described in Section 4.4.

3.1. Thermodynamic framework

The present model is developed in the framework of plasticity and damage mechanics, with non-associative flow rule for damage evolution. Damage mechanics has been widely used for modelling cohesive interfaces [57, 58, 59, 39, 45], as it can properly describe de-cohesion and fracture processes. Several effective interface constitutive models [60, 44, 40, 61, 46] are derived starting from a geometrical definition of the classical scalar damage variable ω as

$$\omega := \frac{dS_c}{dS} = \frac{dS - dS_s}{dS} \tag{1}$$

where, in the proximity of a generic point, dS measures the reference *pristine* interface and dS_c its *failed* or *cracked* fraction.

Since interfaces are used to drive de-cohesion along pre-determined zero-thickness surfaces, the kinematic variable adopted to measure the actual deformation is the *displacement jump* vector across the interface, namely

$$\delta \boldsymbol{u} = \boldsymbol{u}^+ - \boldsymbol{u}^-, \tag{2}$$

where $\boldsymbol{u}^+$ and $\boldsymbol{u}^-$ are the displacements at the upper $(+)$ and lower $(-)$ faces of the opening interface. Later on, in the framework of polycrystalline modelling, such displacement jumps will be associated to couples of homologous intergranular nodes belonging to different but contiguous crystals, in order to formulate suitable sets of interface equations for the aggregate, see Section 4.4.

The discussed formulation defines an extrinsic cohesive model, defined as an elastic-plastic damage model with initial rigid behaviour, although also its intrinsic counterpart has been implemented. Moreover, it assumes the existence of a moving *endurance* surface in the three-dimensional space of the traction components $\{t_1, t_2, t_3\}$, such that no material degradation under cyclic loading happens for traction states within such surface. To comply with thermodynamic principles, a Helmholtz free energy density function per unit surface, playing the role of a potential with respect to both the external and internal state variables, is introduced as

$$\psi(u_i, \alpha_i, \omega) := \frac{1-\omega}{2\,\omega}\left[K_i \left\langle \delta u_i - \delta u_i^p \right\rangle_n^2 + C_i \alpha_i^2\right] + \frac{1}{2} K_i \left\langle \delta u_i - \delta u_i^p \right\rangle_c^2, \tag{3}$$

where $i = 1, 2, 3$, the Einstein's summation convention holds and, in order to take in to account the different behaviour under tensile and compressive normal traction, the operators

$$\langle f_i \rangle_n := \begin{cases} f_i & i = 1, 2 \\ \langle f_3 \rangle_+ \end{cases} \qquad \langle f_i \rangle_c := \begin{cases} 0 & i = 1, 2 \\ \langle f_3 \rangle_- \end{cases} \tag{4}$$

have been employed, with the Macaulay brackets $\langle \cdot \rangle_+$ and $\langle \cdot \rangle_-$ selecting respectively the positive or negative part of their argument. In Eq.(3), K_i denote elastic stiffness components, δu_i are displacement jump components, with $\delta u_3 = \delta u_n$, δu_i^p identify residual displacement components at the interface upon complete un-loading, which can be considered as plastic components in the interface deformation process, C_i are hardening coefficients and α_i are kinematic hardening variables governing the position of the endurance surface.

Thermodynamic consistency, in the form of the second principle, is enforced by the Clausius-Duhem inequality, which gives an explicit form for the non-negative mechanical energy dissipation density as

$$D = t_i \delta \dot{u}_i - \dot{\psi} \geq 0, \tag{5}$$

which upon expansion of the term $\dot{\psi}$, considering the specific form given in Eq.(3), yields

$$D = \left(t_i - \frac{\partial \psi}{\partial \delta u_i}\right) \delta \dot{u}_i - \frac{\partial \psi}{\partial \omega} \dot{\omega} - \frac{\partial \psi}{\partial \delta u_i^p} \delta \dot{u}_i^p - \frac{\partial \psi}{\partial \alpha_i} \dot{\alpha}_i \geq 0. \tag{6}$$

For any purely elastic process, the lack of damage evolution $\dot{\omega} = 0$, of plastic evolution $\dot{\delta} u_i^p = \dot{\alpha}_i = 0$ and of dissipation $D = 0$ imply

$$t_i := \frac{\partial \psi}{\partial \delta u_i} = \frac{1-\omega}{\omega} K_i \left\langle \delta u_i - \delta u_i^p \right\rangle_n + K_i \left\langle \delta u_i - \delta u_i^p \right\rangle_c \tag{7}$$

for $i = 1, 2, 3$, which define the *traction components* t_i as the conjugate of the interface elastic deformations $\delta u_i^e = \delta u_i - \delta u_i^p$. Eqs.(7) will provide part of the intergranular interface equations directly enforced in the polycrystalline aggregate system, as shown in Section 4.4.

For dissipative processes, on the other hand, thermodynamic consistency requires

$$D = Y\dot{\omega} + t_i \delta\dot{u}_i^p - t_i^0 \dot{\alpha}_i \geq 0, \tag{8}$$

obtained from Eq.(6) considering that $-\partial\psi/\partial\delta u_i^p = \partial\psi/\partial\delta u_i = t_i$ and defining the *energy release rate*

$$Y := -\frac{\partial\psi}{\partial\omega} = \frac{1}{2\omega^2}\left[K_i \left\langle \delta u_i - \delta u_i^p \right\rangle_n^2 + C_i \alpha_i^2\right], \tag{9}$$

and the *traction hardening components* t_i^0

$$t_i^0 := \frac{\partial\psi}{\partial\alpha_i} = \frac{1-\omega}{\omega} C_i \alpha_i, \tag{10}$$

which complete the set of state equations. For pristine materials, for which $\omega = 0$, the definition of energy release rate in Eq.(9) is indeterminate. The formal indeterminacy can however be overcome expressing Y as a function of the traction components as

$$Y = \frac{1}{2(1-\omega)^2}\left[K_i^{-1} \left\langle t_i \right\rangle_n^2 + C_i^{-1} {t_i^0}^2\right]. \tag{11}$$

Eq.(8) states that the total dissipation D is given by the sum of a term $Y\dot{\omega}$ energetically related to damage increments, a term $t_i \dot{\delta} u_i^p$ related to the occurrence of plastic mechanisms and a last term $t_i^0 \dot{\alpha}_i$ energetically related to interface microstructural re-organisation during kinematic plastic hardening.

Pure damage evolution and plastic damage evolution are triggered by two different conditions: the pure damage activation condition, which initiates interface softening when the limit strength is attained and the non-associative elasto-plastic damage activation condition, which starts interface degradation under cyclic loading through a coupled plastic-damage activation and evolution function, able to model the interface stiffness and strength degradation under cyclic loads. Such activation conditions and the mechanics of the related processes are described in the next sections.

3.2. Damage activation and evolution

The activation of pure damage at the interfaces is governed by the function

$$\phi_d = \frac{Y}{Y_0} - 1, \tag{12}$$

with Y_0 denoting a constant energy threshold given by

$$Y_0 = \frac{1}{2} K_n^{-1} {t_n^d}^2, \tag{13}$$

where $K_n = K_3$ denotes an interface stiffness-like normal term and t_n^d is the interface *cohesive tensile strength* in the case of pure damage, when no plastic processes are activated.

Under increasing monotonic loading the interface behaves elastically as long as $\phi_d < 0$. When the threshold condition $\phi_d = 0$ is attained, pure damage evolution is triggered, with the following associated flow rules

$$\dot{\omega} = \frac{\partial \phi_d}{\partial Y} \dot{\lambda}_d = \frac{\dot{\lambda}_d}{Y_0}, \tag{14}$$

and loading/un-loading/re-loading conditions

$$\dot{\lambda}_d \geq 0, \qquad \phi_d \, \dot{\lambda}_d = 0, \qquad \dot{\phi}_d \, \dot{\lambda}_d = 0, \tag{15}$$

where $\dot{\lambda}_d$ is the damage multiplier. The dissipation associated with damage evolution can be computed considering that $\dot{\omega} > 0$ only if $\phi_d = 0$, which yields

$$D_d = Y \dot{\omega} = \dot{\lambda}_d \geq 0, \tag{16}$$

showing the unconditioned positiveness of the dissipation rate for any damage increment, being $D_d = 0$ only if $\dot{\lambda}_d = 0$.

In the case of pure damage, i.e. with $\delta u_i^p = 0$, $\alpha = 0$, the proposed cohesive model results in a bilinear response. Employing the expression of Y provided by Eq.(11) into Eq.(12) in the case of pure mode I de-bonding, when $t_n \geq 0$ and $t_t = 0$, yields

$$\phi_d = \frac{1}{(1-\omega)^2} \left(\frac{t_n}{t_n^d} \right)^2 - 1 = 0 \quad \Rightarrow \quad t_n = (1-\omega) t_n^d, \tag{17}$$

which identifies the loading softening branch of the traction-separation relationship and, for a pristine interface, $\omega = 0$, confirms the value of $t_n = t_n^d$ as the traction threshold value for damage activation. On the other hand, using Eq.(9) in the activation condition in Eq.(12), gives

$$\phi_d = \frac{1}{\omega^2} \left(\frac{K_n \delta u_n}{t_n^d} \right)^2 - 1 = 0 \quad \Rightarrow \quad \omega = \frac{K_n \delta u_n}{t_n^d}, \tag{18}$$

which, at complete de-cohesion, i.e. when $\omega = 1$, provides the *critical opening displacement jump* $u_n^d = t_n^d / K_n$.

Under pure mode II loading, employing Eq.(11) in the activation condition in Eq.(12) and enforcing $\omega = 0$ to identify the onset of damage provides for the *tangential strength* $t_t^d = t_n^d\sqrt{K_t/K_n}$. Using Eq.(9) in the activation condition and enforcing $\omega = 1$ to identify the failure condition, provides for the *critical sliding displacement jump*, i.e. at full mode II de-cohesion, $u_t^d = t_n^d/\sqrt{K_n K_t} = u_n^d\sqrt{K_n/K_t} = t_t^d/K_t$.

Such expressions of the critical opening and sliding displacement jumps allow identifying the parameters K_n and K_t appearing in the extrinsic formulation, which do not express the stiffness of the pristine interface, exhbiting initial rigid behaviour. The presence of such parameters cannot be neglected in a thermodynamically consistent formulation, as they allow to consistently define the energy release rate, i.e. the damage conjugate variable, and the relevant damage activation and evolution condition.

Eventually, from the above relationships, it can be shown that

$$G_{\mathrm{I}} = \frac{1}{2}t_n^d u_n^d = \frac{1}{2}t_t^d u_t^d = G_{\mathrm{II}}, \tag{19}$$

i.e. the same fracture toughness is associated to pure mode I and pure mode II failures.

As mentioned, the proposed extrinsic model can reformulated in an intrinsic form, endowing the pristine interface with an initial elastic behaviour, by assuming for it an initial fictitious small value of damage $\omega_0 > 0$. In this case, to preserve the assumed values of strength t_n^d and fracture energy, the energy threshold should to be accordingly re-defined as

$$Y_0 = \frac{K_n^{-1}{t_n^d}^2}{2\left(1-\omega_0\right)^2}. \tag{20}$$

It is highlighted that the damage activation function defined in Eq.(12) governs the evolution of damage at the interface limit strength, whereas the degradation associated with the cyclic loading is accounted for by plastic hysteresis, which is governed by a different activation function, as it will described in Section 3.3.

3.3. Non-associative elastic-plastic-damage activation condition

To account for interface degradation under cyclic loading, related to complex dissipative mechanisms including crystallographic slip, frictional interactions between asperities, micro-cracking etc., a cohesive law with loading/un-loading/re-loading plastic hysteresis and associated damage is proposed.

Plastic hysteresis is modelled by introducing, in the space of tractions $\{t_1 t_2 t_3\}$, the *endurance surface*

$$\phi_p\left(t_i, t_i^0\right) := \sum_{i=1}^{3} \left(\frac{\langle t_i \rangle_n - t_i^0}{r_i} \right)^2 - 1 = 0, \tag{21}$$

such that neither plastic hysteresis nor damage degradation take place for stress states associated to point falling within the surface itself, i.e. for which $\phi_p\left(t_i, t_i^0\right) < 0$.

The limit condition $\phi_p = 0$ defines an ellipsoid in the traction components space, whose principal semi-axes are r_1, r_2 and r_3 and whose centroid is the vector $\boldsymbol{t}^0$, as represented in Fig.(2). The use of tensile normal tractions in Eq.(21) prevents the development of plastic deformations under compressive loading. Often, cohesive laws are assumed as isotropic in the tangential plane $\{t_1 t_2\}$ so that $r_1 = r_2 = r_t$, $K_1 = K_2 = K_t$, $C_1 = C_2 = C_t$ and $r_3 = r_n$, $K_3 = K_n$, $C_3 = C_n$. On the other hand, if the cohesive law is assumed to be fully isotropic, then $r_i = r$, $K_i = K$, $C_i = C$, for $i = 1, 2, 3$.

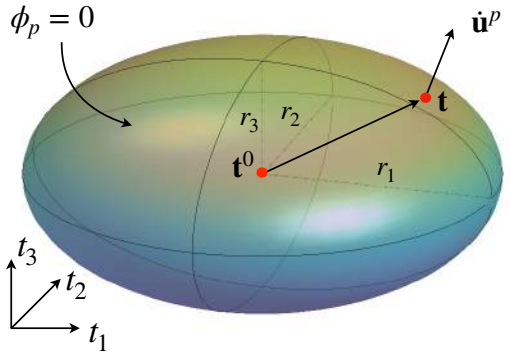

Figure 2: Graphical representation of the endurance elastic-plastic surface in the traction space $\{t_1 t_2 t_3\}$. Plastic evolution takes place ($\dot{\boldsymbol{u}}^p \neq 0$) only when the current traction vector $\boldsymbol{t}$ lies over the surface $\phi_p = 0$.

To model cyclic damage evolution, the proposed formulation is defined in the framework of non-associative damage and plasticity and the following plastic damage potential is assumed to govern the coupled evolution of the plastic and damage variables

$$\Omega_p(t_i, t_i^0, Y) := \sum_{i=1}^{3} \left(\frac{\langle t_i \rangle_n - t_i^0}{r_i} \right)^2 + a \left(\frac{Y}{Y_0} \right)^m, \tag{22}$$

where $a \geq 0$ is the *damage-plasticity coupling parameter*, linking the damage evolution with the hysteresis plastic behaviour and m is the *damage evolution parameter*, affecting the fatigue life of

the interface. The non-associative flow rules are

$$\begin{aligned}
\delta\dot{u}_i^p &= \frac{\partial\Omega_p}{\partial t_i}\dot{\lambda}_p = 2\,\frac{\langle t_i\rangle_n - t_i^0}{r_i^2}\,\dot{\lambda}_p,\\
\dot{\alpha}_i &= -\frac{\partial\Omega_p}{\partial t_i^0}\dot{\lambda}_p = 2\,\frac{\langle t_i\rangle_n - t_i^0}{r_i^2}\,\dot{\lambda}_p,\\
\dot{\omega} &= \frac{\partial\Omega_p}{\partial Y}\dot{\lambda}_p = \frac{am}{Y_0}\left(\frac{Y}{Y_0}\right)^{m-1}\dot{\lambda}_p \geq 0,
\end{aligned} \tag{23}$$

while the loading/un-loading/re-loading conditions read

$$\dot{\lambda}_p \geq 0, \quad \phi_p\dot{\lambda}_p = 0, \quad \dot{\phi}_p\dot{\lambda}_p = 0, \tag{24}$$

where $i = 1, 2, 3$ and $\dot{\lambda}_p$ is the plastic multiplier.

The damage rate can be written as a function of the traction components by substitution of Eq.(11) and Eq.(13) into the third of Eqs.(23). For an interface subjected to tensile normal tractions only, the damage rate assumes the form

$$\dot{\omega} = \frac{am}{Y_0}\left[\frac{t_n^2 + {t_n^0}^2 K_n/C_n}{(1-\omega)^2\,{t_n^d}^2}\right]^{m-1}\dot{\lambda}_p \tag{25}$$

where the hardening component t_n^0 can be considered as the mean stress of the loading cycle. The integration of the damage rate over the loading cycle yields a power expression for the value of the damage increment per cycle analogous to expressions used e.g. in Refs.[62, 30] to model fatigue life in a continuum damage model.

The damage rate defined by the third of Eqs.(23) implies a strong dependence of the damage increments on the damage evolution parameter m: for relatively high values of m, the damage increments are negligible at low stress levels, when $t_n \ll t_n^d$; on the other hand, for $m = 1$ the damage increment is independent on the stress level.

The dissipation associated with the plasticity-damage activation can be computed from Eq.(8) by considering that the flow rules give $\delta\dot{u}_i^p = \dot{\alpha}_i \neq 0$ and $\dot{\omega} > 0$ only if $\phi_p = 0$. Taking into account such conditions and substituting the other terms in Eqs.(23) into Eq.(8) yields

$$D_p = \left[2\sum_{i=1}^{3}\left(\frac{\langle t_i\rangle_n - t_i^0}{r_i}\right)^2 + am\left(\frac{Y}{Y_0}\right)^m\right]\dot{\lambda}_p = \left[2 + am\left(\frac{Y}{Y_0}\right)^m\right]\dot{\lambda}_p \geq 0, \tag{26}$$

which shows the unconditioned positiveness of the dissipation rate for any plastic-damage increment, being $D_p = 0$ only if $\dot{\lambda}_p = 0$.

3.4. Elastic-plastic limit condition

The elastic-plastic endurance surface models the elastic-plastic cyclic behaviour associating to it some definite damage evolution, i.e. elastic degradation, both in the loading path and in the unloading one. The softening behaviour at the limit condition is modelled by the activation of both the two yielding conditions provided by the damage limit condition $\phi_d = 0$ and the elastic-plastic activation condition $\phi_p = 0$.

The evolution of plastic deformation and kinematic hardening is still governed by Eqs.(23), while the evolution of damage is now controlled by the sum of two different terms, namely the damage limit condition and the elastic-plastic activation condition, i.e.

$$\dot{\omega} = \frac{\partial \Omega_p}{\partial Y}\dot{\lambda}_p + \frac{\partial \phi_d}{\partial Y}\dot{\lambda}_d = \frac{am}{Y_0}\left(\frac{Y}{Y_0}\right)^{m-1}\dot{\lambda}_p + \frac{1}{Y_0}\dot{\lambda}_d \geq 0, \tag{27}$$

while the loading/un-loading/re-loading conditions read

$$\begin{aligned} &\dot{\lambda}_p \geq 0, \quad \phi_p \dot{\lambda}_p = 0, \quad \dot{\phi}_p \dot{\lambda}_p = 0, \\ &\dot{\lambda}_d \geq 0, \quad \phi_d \dot{\lambda}_d = 0, \quad \dot{\phi}_d \dot{\lambda}_d = 0. \end{aligned} \tag{28}$$

It is worth noting that, for high values of the fatigue parameter m in Eq.(22), softening can be activated without activation of the damage limit condition, that is for $\phi_d < 0$.

3.5. Graphical description

The traction-separation response of the proposed coupled model to monotonic increasing loading is qualitatively represented in Fig.(3), where it is also compared with the response of the pure damage model, both in the case of extrinsic and intrinsic formulation. The monotonic response is qualitatively the same in pure mode I and pure mode II loading and it may exhibit either initial rigid behaviour, as in the case of extrinsic implementation, or initial elastic behaviour with finite stiffness, in the case of intrinsic implementation.

The condition $\phi_p = 0$ activates an elastic-plastic process at the interface, with an associated damage rate that induces cycle-by-cycle interface degradation, as schematically described in Figs.(4a,b). In particular, Fig.(4a) represents the first activation of the plastic behaviour of the pristine interface, with the endurance surface centred at the origin of the traction space, and increment of plastic deformation accompanied by stiffness and strength degradation due to the the small increment of damage produced by the coupled plastic-damage model. Fig.(4b) shows the elastic unloading with

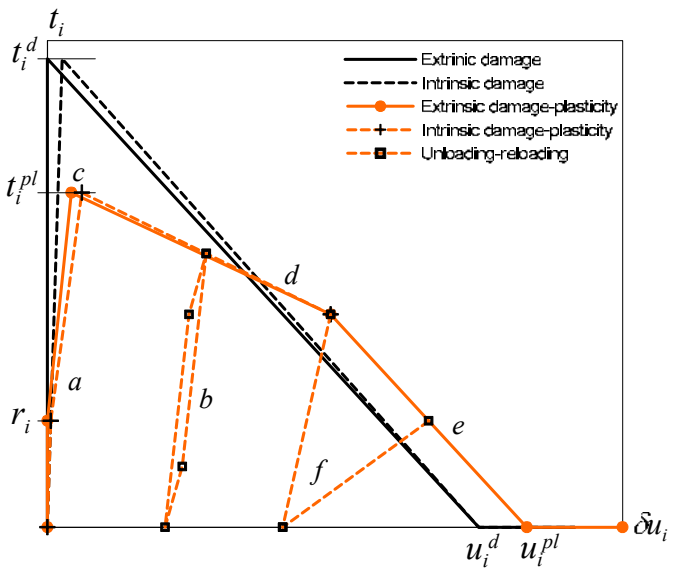

Figure 3: Pure mode I (or II) interface traction-separation response for a monotonic increasing load. The marked branches, identified by the letters *a*-*f* and corresponding to different physical behaviours (elastic; elastic-plastic with degradation; elastic-plastic-damage with softening; damage with softening; unloading-reloading) are schematically described/discussed in Fig.(4).

traction inside the endurance surface and the subsequent plasticity-damage activation in the unloading branch.

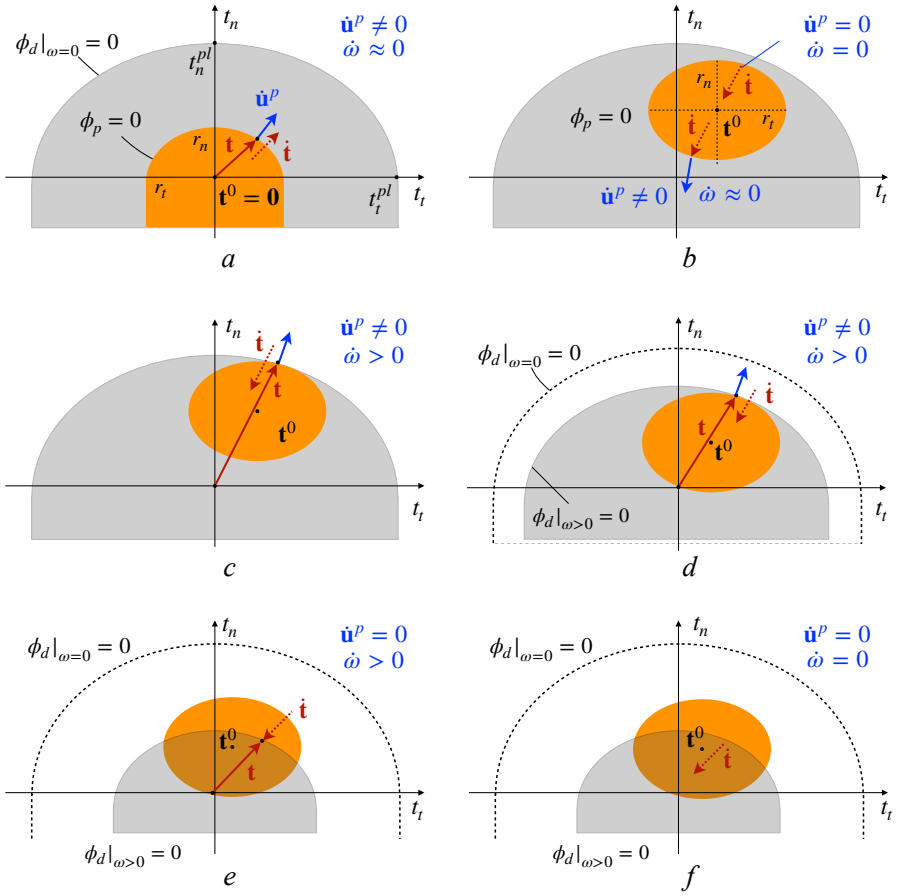

Figure 4: Qualitative representation of the interface behaviour in the plane of normal and tangential tractions: a) first plastic activation of the pristine material with fatigue elastic degradation; b) elastic unloading and subsequent plastic activation with fatigue degradation; c) plastic and damage activation functions are both attained at the maximum strength; d) softening branch with plastic and damage increments; e) damage softening with null plastic increments; f) elastic unloading of the damaged material with traction inside the endurance surface.

The interface *elastic-plastic strength* t_i^{pl} is reached when both the threshold conditions $\phi_p = 0$ and $\phi_d = 0$ are attained, see Figs.(4c,d). Under monotonically increasing load, the condition $\phi_p = 0$ may be reached first; the subsequent attainment of the condition $\phi_d = 0$ then activates material softening, with the related interface stiffness and strength degradation up to complete de-cohesion.

However, for high values of the exponent m, the interface may exhibit softening even before the quasi-static damage activation condition $\phi_d = 0$ is fulfilled, which is the expedient used to model degradation under cyclic loading.

In a fatigue test under load control, with traction levels below the maximum strength, the activation of the plastic limit condition $\phi_p = 0$ induces small damage increments with subsequent strength degradation, due to the increase of the energy release rate in Eq.(11) and the increase of the damage limit function in Eq.(12). Eventually, the attainment of the damage limit condition $\phi_d = 0$ triggers the direct evolution of damage up to interface failure.

The ultimate strength modelled by the proposed formulation is governed by pure damage softening, represented by the branch e in Fig.(3), associated to tractions and damage levels internal to the endurance surface ($\phi_p < 0$) and which attain the damage activation function ($\phi_d = 0$), as represented in the Fig.(4e). In fact, damage increments induce isotropic softening, corresponding to the shrinking of the volume enclosed by the damage activation function in the tractions space, whereas the plastic activation function, which is not directly influenced by the damage parameter, can only undergo kinematic hardening. So, for high damage levels, the plastic activation surface ($\phi_p = 0$) is not contained within the damage activation surface, which shrinks up to degenerating into a point as the failure damage condition $\omega = 1$ is reached. Pure damage softening is associated to the pure elastic unloading represented by the branch f in Fig.(3) and with the traction path schematically represented in the Fig.(4f).

The elastic-plastic response of the interface is generally path dependent and cannot be analytically evaluated. Nevertheless, if in monotonic loading the damage developed in the initial elastic-plastic branch is neglected, the interface strength t_i^{pl} can be estimated by enforcing the conditions $\phi_p = 0$, $\phi_d = 0$ and $\omega = 0$. In this case, the interface elastic-plastic strength can be approximated as

$$t_n^{pl} \approx \frac{r_n K_n + \sqrt{r_n K_n + (K_n + C_n)\left({t_n^d}^2 C_n - r_n^2 K_n\right)}}{K_n + C_n} \tag{29}$$

in pure mode I loading and as

$$t_t^{pl} \approx \frac{r_t K_t + \sqrt{r_t K_t + (K_t + C_t)\left({t_t^d}^2 C_t - r_t^2 K_t\right)}}{K_t + C_t} \tag{30}$$

for pure mode II loading.

In conclusion, considering again that, upon progressive monotonic loading, the energy dissipated in plastic processes is negligible with respect to the energy dissipated in damaging processes, and thus assuming a bilinear response upon monotonic opening loading up to complete de-cohesion, the mode I *critical elastic-plastic opening displacement* can be approximated as $u_n^{pl} \approx 2G_{\mathrm{I}}/t_n^{pl}$, where Eq.(13) has been employed. Similar considerations apply in mode II.

4. Polycrystalline boundary element framework

In this section, the key aspects of the developed framework for the analysis of polycrystalline microstructures are described. The framework is based on the use of boundary integral equations for the description of the mechanics of individual grains, whose artificial morphology is generated through Laguerre-Voronoi tessellations, as described in Section 2. The employment of such boundary integral equations, their suitable discretisation and subsequent numerical treatment produce a system of equations that can be readily interfaced with the cohesive laws developed above, demonstrating the flexibility of the underlying framework in accommodating different degradation mechanisms.

4.1. Meshing of artificial polycrystalline morphologies

As mentioned in Section 2, polycrystalline morphologies are represented in this work through Laguerre-Voronoi tessellations, in which each grain g is a convex polyhedron with volume V^g enclosed by the boundary B^g, given by the union of flat and convex polygonal faces

$$B^g = \partial V^g = \bigcup_{n=1}^{N_f^g} F_n^g, \tag{31}$$

where F_n^g is the generic *n-th* face of the grain and N_f^g denotes the total number of faces of the grain g. To simplify the expression of boundary and interface conditions, local reference systems are attached to each grain face: such reference systems vary over the grain boundary and allow to express the mechanical fields into face normal and tangential components. The morphology of a generic grain and the definition of face-local reference systems are illustrated in Fig.(5a).

Since boundary integral equations are employed to represent the mechanics of individual grains, as it will be shown in next Section, the numerical treatment of the polycrystalline problem requires the meshing of the grains surfaces only, at least in the case in which non-linear phenomena are

confined at the intergranular interfaces and may be neglected in the grains interior, as assumed here. Considered the statistical nature of polycrystalline tessellations, which implies high variability in the morphology of individual grains, the possibility of analysing their mechanics employing boundary meshes only constitutes a relevant simplification of pre-processing and contributes to the robustness of the scheme.

In the present contribution, the grains surface mesh is generated according to the procedure developed in Ref.[21]: each convex polygonal face F_n^g is subdivided into a collection of non-overlapping triangular and quadrangular, continuous and semi-discontinuous elements e_k, as shown in Fig.(5b). Semi-discontinuous elements are employed to avoid some complexities arising in boundary element formulations when nodes are collocated on edges where the surface normal is not unambiguously defined [63], as in the case of grains edges where two contiguous faces meet. The mesh size is selected so that $\xi_e \ll L_{cz}$ [16, 20], where ξ_e represents the average element size and L_{cz} is the cohesive zone size at the intergranular interfaces, which can be estimated in terms of the material fracture toughness and the interface strength [64, 10, 65]. As discussed and computationally tested in Refs.[16, 20, 21], such a choice ensures the *mesh-independency* and *reproducibility* of the aggregate macro-response.

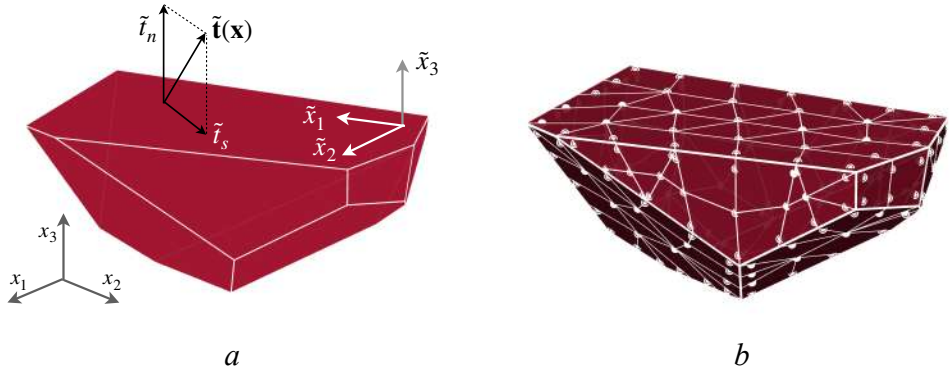

Figure 5: Example grain morphology and mesh: *a*) each grain is a convex polyhedron bounded by flat convex polygonal faces; each face carries its own local reference system $\{\tilde{x}_1\tilde{x}_2\tilde{x}_3\}$, differing from the global reference system $\{x_1x_2x_3\}$, which allows the decomposition of boundary displacements and tractions into normal and tangential components; *b*) each grain face is meshed into non-overlapping triangular or quadrangular elements.

4.2. Boundary integral equations for the individual grains

The polycrystalline boundary element framework is based on the integral representation of the microstructural displacement field. In particular, considered a generic point $\boldsymbol{x} \in B^g$, under the assumption of linear elastic behaviour of the grains, it is possible to express its displacements resorting to the integral representation

$$\tilde{c}_{ij}^{\,g}(\boldsymbol{x})\tilde{u}_j^{\,g}(\boldsymbol{x}) + \sum_{n=1}^{N_f^g} \fint_{F_n^g} \tilde{T}_{ij}^{\,g}(\boldsymbol{x},\boldsymbol{y})\tilde{u}_j^{\,g}(\boldsymbol{y})\mathrm{d}S(\boldsymbol{y}) = \sum_{n=1}^{N_f^g} \int_{F_n^g} \tilde{U}_{ij}^{\,g}(\boldsymbol{x},\boldsymbol{y})\tilde{t}_j^{\,g}(\boldsymbol{y})\mathrm{d}S(\boldsymbol{y}), \tag{32}$$

with $i,j = 1,2,3$. Eq.(32) expresses the displacement components $\tilde{u}_j^{\,g}$ at the generic boundary *collocation point* $\boldsymbol{x}$ in terms of the displacements $\tilde{u}_j^{\,g}(\boldsymbol{y})$ and tractions $\tilde{t}_j^{\,g}(\boldsymbol{y})$ over the boundary B^g itself, with $\boldsymbol{y} \in B^g$ being the generic *integration point*, spanning the boundary of the considered grain in the integration procedure. The symbol $\fint$ denotes the integral Cauchy principal value, necessary to identify the value of the improper integral when integration is performed over an element containing the collocation point; the over-tilde $\tilde{\cdot}$ denotes vector components expressed with respect to the *local* reference systems, attached to *each* grain face F_n^g and then varying as the integration point spans the grains boundary, see e.g. Refs.[66, 20] and Fig.(5b). $\tilde{U}_{ij}^{\,g}(\boldsymbol{x},\boldsymbol{y})$ and $\tilde{T}_{ij}^{\,g}(\boldsymbol{x},\boldsymbol{y})$ are rotated components of the 3D anisotropic fundamental solutions of the grain material, computed as in Ref.[67]. Eventually, $\tilde{c}_{ij}^{\,g}(\boldsymbol{x})$ are *free terms*, arising from the boundary limiting procedure and depend on the smoothness of the boundary B^g at the collocation point $\boldsymbol{x}$.

For further details about the boundary integral representation of mechanical problems and their numerical treatment within the framework of the boundary element method, interested readers are referred to Refs. [14, 15].

4.3. Numerical integration of the boundary integral equations

Once a suitable artificial tessellation is available, the computational treatment of the polycrystalline problem is addressed according to the following scheme:

- Each grain g is discretised by subdividing its faces F_n^g into a collection of non-overlapping boundary elements e_k, as recalled in Section 4.1 and explained in Ref.[21];
- Over each element e_k, the local geometry is expressed through shape functions $\mathbf{N}_e\left(\eta_1,\eta_2\right)$ and the coordinates of the element vertices, while the boundary displacement and traction fields

are expressed through shape functions and nodal values of boundary displacements $\tilde{\mathbf{U}}^g_{e_k}$ and tractions $\tilde{\mathbf{T}}^g_{e_k}$, defined with respect to locally defined 2D (surface) coordinate systems (η_1, η_2);

- Eq.(32) is *collocated* at each grain boundary node and it is numerically integrated, taking into account the approximation of the boundary fields in terms of shape functions and nodal values, as detailed in Ref.[21].

As an example, considering the left-hand side of Eq.(32) and remembering that, after the discretisation $\boldsymbol{y} = \boldsymbol{y}(\boldsymbol{\eta})$, $\boldsymbol{u} = \boldsymbol{u}(\boldsymbol{\eta})$ and $\boldsymbol{t} = \boldsymbol{t}(\boldsymbol{\eta})$, the above procedure yields for *each* face F^g_n

$$\int_{F^g_n} \tilde{T}^g_{ij}(\boldsymbol{x}, \boldsymbol{\eta}) \tilde{u}^g_j(\boldsymbol{\eta}) \mathrm{d}S(\boldsymbol{\eta}) = \sum_{k=1}^{N^F_e} \underbrace{\left[\int_{e_k} \tilde{T}^g_{ij}(\boldsymbol{x}, \boldsymbol{\eta}) \mathbf{N}_e(\boldsymbol{\eta}) J(\boldsymbol{\eta}) \mathrm{d}\eta_1 \mathrm{d}\eta_2 \right]}_{\mathbf{H} \text{ matrix block}} \cdot \tilde{\mathbf{U}}^g_{e_k}, \tag{33}$$

where e_k identifies the element over which the integration is being performed, N^F_e is the number of boundary elements belonging to the considered face after the subdivision process, $J(\boldsymbol{\eta})$ is the Jacobian of the coordinates transformation $\boldsymbol{y} = \boldsymbol{y}(\boldsymbol{\eta})$ computed at $\boldsymbol{\eta}$ and the vector $\tilde{\mathbf{U}}^g_{e_k}$ groups the components of displacements associated with the nodes belonging to the element e_k. The integral can be numerically computed employing suitable quadrature rules and produces, after the integration, a matrix block contributing to the population of a larger matrix $\mathbf{H}^g$, associated with the considered grain and multiplying the components of nodal boundary displacements associated with it.

Analogously, the integration of the terms appearing at the right-hand side of Eq.(32) produces terms of the form

$$\int_{F^g_n} \tilde{U}^g_{ij}(\boldsymbol{x}, \boldsymbol{\eta}) \tilde{t}^g_j(\boldsymbol{\eta}) \mathrm{d}S(\boldsymbol{\eta}) = \sum_{k=1}^{N^F_e} \underbrace{\left[\int_{e_k} \tilde{U}^g_{ij}(\boldsymbol{x}, \boldsymbol{\eta}) \mathbf{N}_e(\boldsymbol{\eta}) J(\boldsymbol{\eta}) \mathrm{d}\eta_1 \mathrm{d}\eta_2 \right]}_{\mathbf{G} \text{ matrix block}} \cdot \tilde{\mathbf{T}}^g_{e_k}, \tag{34}$$

i.e. matrix blocks contributing to the population of a larger matrix $\mathbf{G}^g$ associated with the considered grain and multiplying the components of nodal boundary tractions relative to its nodes, whose terms associated with the element e_k appear in $\tilde{\mathbf{T}}^g_{e_k}$.

It is worth noting that Eq.(32), when collocated at a defined boundary node, allows computing three rows of the mentioned matrices $\mathbf{H}^g$ and $\mathbf{G}^g$: to populate the entire matrices, the equation must be sequentially collocated over all the nodes identified during the geometrical discretisation and meshing procedure. In the integration procedure, here briefly recalled, care must be used in the

numerical integration of the elements containing the collocation point, as they give rise to *singular integrals*. For a deeper consideration of such aspects, interested readers are referred to Refs. [14, 15].

In conclusion, the above scheme leads, for each grain, to the system

$$\mathbf{H}^g \cdot \tilde{\mathbf{U}}^g = \mathbf{G}^g \cdot \tilde{\mathbf{T}}^g, \tag{35}$$

expressed in terms of the vectors $\tilde{\mathbf{U}}^g, \tilde{\mathbf{T}}^g \in \mathbb{R}^{3N_p^g}$, collecting the components of boundary displacements and tractions of all the grain nodes, with $\mathbf{H}^g, \mathbf{G}^g \in \mathbb{R}^{3N_p^g \times 3N_p^g}$, where N_p^g is the number of nodes associated with the grain g.

4.4. Aggregate system and solution

After boundary element discretisation and numerical integration of the boundary integral equations collocated at the boundary nodes, a system of the form given in Eq.(35) is associated to each grain within the aggregate: such systems are expressed in terms of the components of displacements and tractions of the mesh boundary nodes identified during the meshing procedure recalled in Section 4.1. It is important to realise that all the components of displacements and tractions appear in the vectors $\tilde{\mathbf{U}}^g$ and $\tilde{\mathbf{T}}^g$ and no reference to external boundary conditions and/or interface conditions has been made so far. However, restoring the integrity of the aggregate, from the mathematical point of view, entails precisely the enforcement of boundary and interface conditions.

In order to apply the relevant boundary conditions, it is important to distinguish between *boundary* and *internal* grains: the former have one or more faces lying over the external boundary of the aggregate B, while the latter are entirely surrounded by other grains. The boundary conditions are applied only over the faces of the boundary grains lying on B, following the standard subdivision into known and unknown components. For the boundary grains, the enforcement of the external boundary conditions transforms system (35) into

$$\mathbf{A}^g \cdot \mathbf{X}^g = \mathbf{B}^g \cdot \mathbf{Y}^g \tag{36}$$

where the vectors $\mathbf{X}^g$ and $\mathbf{Y}^g$ collect respectively *unknown* and *prescribed* values of grain-boundary displacements and tractions, while the matrices $\mathbf{A}^g$ and $\mathbf{B}^g$ collect columns from $\mathbf{H}^g$ and $\mathbf{G}^g$ corresponding to the above unknown and prescribed degrees of freedom [15].

Considering an artificial aggregate consisting of N_g grains, the systems of the form given in

Eq.(36), associated to each grain, can be collected in a unique aggregate system as

$$\begin{bmatrix} \mathbf{A}^1 & \mathbf{0} & \cdots & \mathbf{0} \\ \mathbf{0} & \mathbf{A}^2 & \cdots & \mathbf{0} \\ \vdots & \vdots & \ddots & \vdots \\ \mathbf{0} & \mathbf{0} & \cdots & \mathbf{A}^{N_g} \end{bmatrix} \cdot \begin{bmatrix} \mathbf{X}^1 \\ \mathbf{X}^2 \\ \vdots \\ \mathbf{X}^{N_g} \end{bmatrix} = \begin{bmatrix} \mathbf{B}^1 & \mathbf{0} & \cdots & \mathbf{0} \\ \mathbf{0} & \mathbf{B}^2 & \cdots & \mathbf{0} \\ \vdots & \vdots & \ddots & \vdots \\ \mathbf{0} & \mathbf{0} & \cdots & \mathbf{B}^{N_g} \end{bmatrix} \cdot \begin{bmatrix} \mathbf{Y}^1 \\ \mathbf{Y}^2 \\ \vdots \\ \mathbf{Y}^{N_g} \end{bmatrix}, \tag{37}$$

which implements the boundary conditions, but not the interface equations yet.

The interface conditions can be enforced considering that they establish *i*) an equilibrium relationship between the traction components of conformal nodes belonging to contiguous grains and *ii*) a relationship between tractions and intergranular displacement jumps (interface opening) of couples of homologous nodes (interface pairs). To avoid confusion, it is important to realise here that the geometric point $\boldsymbol{x} \in I^{ab}$, where I^{ab} is the interface between the grains a and b, identifies the location in space where the *physical* points $\boldsymbol{x}^a \in a$ and $\boldsymbol{x}^b \in b$ meet in the initial undeformed configuration. As the loading progresses, generally $\boldsymbol{x}^a \neq \boldsymbol{x}^b$ and $\boldsymbol{x}^b - \boldsymbol{x}^a = \delta\boldsymbol{u}^{ab}$, where $\delta\boldsymbol{u}^{ab}$ defines the displacement *jump* associated with the pair identified by the initial location $\boldsymbol{x}$.

Given this premise, the tractions equilibrium at the generic initial interface point $\boldsymbol{x} \in I^{ab}$ can be readily enforced as

$$\tilde{t}_i^a(\boldsymbol{x}) = \tilde{t}_i^b(\boldsymbol{x}) \qquad \forall \boldsymbol{x} \in I^{ab}, \tag{38}$$

where $\tilde{t}_i^g(\boldsymbol{x})$ denotes the *i-th* traction component associated with the node $\boldsymbol{x}^g \in g$, such that $\boldsymbol{x}^g \equiv \boldsymbol{x}$ in the undeformed state, and the signs in the equations are determined by the fact that the traction components associated to points belonging to contiguous faces of neighbour grains are expressed in local systems that are *opposite* to each other. The equilibrium conditions in Eq.(38), three for each interface node pair, form part of the interface equations: *their form never changes* during the aggregate evolution, as the equilibrium holds also for damaged or failed interface regions.

On the other hand, as detailed in Section 3, interface tractions and displacement jumps are linked by the cohesive traction-separation laws. At a generic step during the loading process, for a generic interface pair identified by $\boldsymbol{x} \in I^{ab}$ the traction-separation link can be expressed as in Eq.(7), i.e., more generally as

$$\tilde{t}_i\left(\boldsymbol{x}\right) = t_i\left(\boldsymbol{x}, \delta\tilde{\boldsymbol{u}}, \delta\tilde{\boldsymbol{u}}^p, \omega\right), \tag{39}$$

where the symbols have the meaning discussed in Section 3 and the tilde has been added to indicate components expressed in the local reference systems.

At this point, all the ingredients are in place to write the aggregate equations, which are comprised of Eqs.(37-39) and can be recast in the compact form

$$\left[\begin{array}{c} \mathbf{A} \cdot \mathbf{X} \\ \mathbf{I}\left(\mathbf{X}, \delta\mathbf{X}, \delta\mathbf{U}^p, \boldsymbol{\omega}\right) \end{array} \right] = \left\{ \begin{array}{c} \mathbf{B} \cdot \mathbf{Y}(\lambda) \\ \mathbf{0} \end{array} \right\}, \tag{40}$$

where the matrices $\mathbf{A}$ and $\mathbf{B}$ are the coefficient matrices defined in Eq.(37); the matrix block $\mathbf{I}$ implements Eqs.(38-39); the vector $\mathbf{X}$ contains, as already mentioned, the *unknown* components of grain-boundary nodal displacements $\tilde{u}_i$ and tractions $\tilde{t}_i$, which are the primary variables of the formulation, while $\mathbf{Y}(\lambda)$ contains the *known* components of nodal displacements and tractions, which depend on the load factor λ that can also be associated with a time variable, as in the present study; the vector $\boldsymbol{\omega}$ collects the components ω_k expressing the local total interface degradation at the generic interface node pair k and, eventually, the vector $\delta\mathbf{U}^p$ collects all the residual displacements at the interface.

4.5. Incremental iterative solution of the polycrystalline system

For its effective solution, system (40) must be considered, within the framework of a consistent incremental-iterative solver, together with the damage activation and yield conditions, the damage and plastic flow rules and the loading, unloading/reloading conditions given and discussed in Section 3. The system can be re-written in compact form as

$$\mathbf{M}\left(\mathbf{X}, \delta\mathbf{X}, \delta\mathbf{U}^p, \boldsymbol{\omega}\right) = \mathbf{Z}\left(\lambda\right), \tag{41}$$

in which the micro-structural evolution is triggered by the cyclic loading, generally expressed in terms of the load factor λ. The micro-evolution is tracked by solving the boundary value problem for a discrete set of values λ_k: once the solution $\mathbf{X}_k$ corresponding to λ_k is known, a new load increment $\Delta\lambda_k$ is applied and the new solution $\mathbf{X}_{k+1}$ corresponding to $\lambda_{k+1} = \lambda_k + \Delta\lambda_k$ is sought using a Newton-Raphson algorithm for solving system (41).

Since the matrix $\mathbf{M}\left(\mathbf{X}, \delta\mathbf{X}, \delta\mathbf{U}^p, \boldsymbol{\omega}\right)$ is sparse, the iterative solution of Eq.(41) is performed using the solver `PARDISO` (`http://www.pardiso-project.org/`). In the solution of Eq.(41), which stems from a boundary element collocation procedure, higher computational efficiency could be attained using Krylov iterative solvers in conjunction with special matrix representations, obtained for example using fast multipoles [68] or hierarchical matrices [69, 70, 71].

5. Computational experiments

In this section, the developed framework is computationally tested. The proposed cohesive laws are first assessed by analysing the quasi-static and low-cycle behaviour of a single interface between two quasi-rigid prismatic grains, modelled with the boundary element method. Then, the response of few polycrystalline aggregates of elastic grains subjected to different kinds of boundary conditions is simulated: both fully-3D and pseudo-3D aggregates are considered, to illustrate the potential of the method both in a multiscale perspective and in micro-mechanical applications, e.g. in the analysis of MEMS.

All the reported tests have been performed by fulfilling the criteria on the mesh-size mentioned in Section 4.1, which ensure mesh-independency and reproducibility of the aggregate macro-response, which has also been preliminarily assessed and validated.

5.1. Grains and interfaces properties

As mentioned above, both elastic and quasi-rigid grains are considered, for different purposes, in the performed tests. In the first case, the considered material is *polysilicon*, often used in the manufacturing of MEMS: the individual grains present cubic material symmetry with independent elastic constants $c_{11} = 166\,\text{GPa}$, $c_{12} = 64\,\text{GPa}$ and $c_{44} = 79.6\,\text{GPa}$, according to Ref.[72].

On the other hand, in all the considered tests, the intergranular interfaces are fully defined by the properties reported in Table 1, estimated as follows. The value of the elastic-plastic mode I strength t_n^{pl} is related to the material's macroscopic static strength σ_c, analogously to what was assumed in previous works for the interface cohesive strength, see e.g. Refs.[20, 22]. However, it is known that the static strength of brittle materials, such as polysilicon, exhibits significant scatter [73, 74]: in this study it is assumed that $t_n^{pl} = \sigma_c = 1.1\,\text{GPa}$, consistent with the values of σ_c reported in Ref.[75].

The critical mode I displacement jump u_n^{pl} is estimated by considering that G_I is the *work of separation* per unit surface, i.e. the energy spent per unit surface to take an initially pristine interface to complete de-cohesion; since, in the limit case of quasi-static monotonic loading, the proposed law describes an approximately bi-linear path, it is possible to write

$$G_I = \frac{1}{2}\, t_n^d\, u_n^d \approx \frac{1}{2}\, t_n^{pl}\, u_n^{pl}, \tag{42}$$

from which u_n^{pl} can be approximately estimated. If not readily available, G_I can be computed as

$$G_I = \frac{\left(1-\nu^2\right) K_I^2}{E}, \tag{43}$$

where K_I, E and ν are the *fracture toughness* and Young and Poisson moduli of the the bulk material, see e.g. Ref.[76]. With *bulk material* we refer here to the macro-material considered as homogeneous, whose properties emerge from the interactions of the grains at the micro-scale and can be estimated through suitable homogenisation. In this contribution, for polysilicon it is assumed $K_I = 1.1\,\mathrm{MPa}\sqrt{\mathrm{m}}$, consistently with the values reported in Ref.[77]; on the other hand, $E = 163\,\mathrm{GPa}$ and $\nu = 0.22$ are the assumed elastic constants of bulk polysilicon, estimated from the Hashin–Shtrikman bounds [78] of an untextured aggregate of individual crystals whose elastic constants c_{11}, c_{12} and c_{44} have the values reported above.

The endurance surface diameter $d_n = 2\,r_n$ can be estimated considering that, in the proposed cohesive law, no cyclic degradation occurs when the traction vector remains within the endurance surface itself, see Fig.(2). In this work, such a diameter has been conventionally determined referring to the stress amplitude of a cyclic *repeated* stress corresponding to a fatigue lifetime of $N_f \approx 10^9$ cycles: for polysilicon Ref.[75] reports, in this sense, an experimental value of $\Delta\sigma = 0.7\,\mathrm{GPa}$, which implies that, under cyclic repeated stress ranging in the interval $0 \leq \sigma(t) \leq \Delta\sigma$ (only tensile loading without compression), polysilicon exhibits a fatigue life of $N_f \approx 10^9$ cycles. This observation allows setting $d_n = 2\,r_n = \Delta\sigma = 0.7\,\mathrm{GPa}$. Some additional considerations may be useful to avoid confusion: when the interface is pristine, the endurance surface is centred at the point $\boldsymbol{t}^0 = \mathbf{0}$; upon loading, during the first loading cycle, when the traction acting at the interface overcomes the *radius* r_n, it triggers the accumulation of cyclic degradation, as signalled by the change of slope in the ascending branch of the monotonic plastic-damage curve in Fig.(3), which seems contrasting the meaning of the selection of $d_n = 2\,r_n$. However, it should be considered that such a loading also activates kinematic hardening, which translates the endurance surface so that a loading cycle with an effective traction satisfying the condition $0 \leq t \leq d_n$ will always remain within the surface itself, after a very limited and negligible initial accumulation of cyclic damage.

Once t_n^{pl}, u_n^{pl} and r_n are estimated, the remaining interface parameters can be calibrated as follows. Remembering that $t_n^d = K_n u_n^d$ and $t_n^d\, u_n^d = 2G_I$ allows writing $t_n^d = \sqrt{2K_n G_I}$, where K_n should not be confused with K_I. Using this expression in Eq.(29), remembering that r_n has already been estimated, provides a relationship of the form $t_n^{pl} = t_n^{pl}(K_n, C_n)$. At this point, assuming

$C_n = K_n$, for reasons clarified further on, provides a relationship of the form $t_n^{pl} = t_n^{pl}(K_n)$, from which the value of K_n ensuring the previously selected value of t_n^{pl} can be inferred. The hardening coefficient has been set as $C_n = K_n$ so that, in the monotonic plastic-damage curve in Fig.(3), the slope of the curve following the linear loading branch is approximately half that of the linear branch. However, it is underlined that this is an assumption motivated by experimental ignorance: the constant could and should be calibrated from data about the monotoning loading, whenever available. As K_n and C_n are available, the relationships recalled above allow the straightforward determination of t^d abd u_n^d. Moreover, the condition $G_I = G_{II}$ and the assumptions $r_t = r_n$, $K_t = K_n$, $C_t = C_n$ allow determining t_t^{pl}, u_t^{pl}, t_t^d and u_t^d, as summarised in Table 1. It is underlined that the coincidence between normal and tangential components, in Table 1, is motivated by the lack of specific material information and it is not related to a limitation of the cohesive model, which is able to account for differences between normal and tangential values.

Table 1: Intergranular properties for the simulated polycrystalline components.

Property	Component	Value
Interface limit tractions and displacement jumps		
Elastic-plastic limit strengths	t_n^{pl}, t_t^{pl}	1.1 GPa
Elastic-plastic critical displacement jumps	u_n^{pl}, u_t^{pl}	12.84×10^{-3} µm
Pure damage strengths	t_n^d, t_t^d	1.54 GPa
Pure damage critical displacement jumps	u_n^d, u_t^d	9.16×10^{-3} µm
Interface constitutive parameters		
Endurance surface radii	r_n, r_t	0.35 GPa
Cohesive elastic stiffnesses	K_n, K_t	16.83 N µm^{-3}
Cohesive hardening coefficients	C_n, C_t	16.83 N µm^{-3}
Damage-plasticity coupling parameter	a	15
Damage evolution parameter	m	12

The damage evolution parameter m and the coupling parameter a are closely related to the fatigue life of the considered material. In fact, by considering Eq.(25) and Eq.(29), for a uniaxial

tension test the number of cycles to rupture N_f can be estimated as

$$N_f \propto a \left(\frac{t_a^2 + t_m^2}{{t_n^{pl}}^2} \right)^{-(m-1)} \tag{44}$$

where t_a and t_m are the amplitude and mean value of the normal traction cycle. In Ref.[75] the fatigue life of polysilicon tensile specimens was estimated as $N_f = \left(t_a/t_n^{pl}\right)^{-50}$ (where the symbols have been adapted for the sake of readability within the present discussion), which appeared to accurately reproduce the experimental results available to the authors therein. In the present study, the values $m = 12$ and $a = 15$ have been selected by calibrating the cohesive law so to numerically reproduce the same fatigue life as that experimentally observed in Ref.[75], for the values of traction amplitude $t_a = 1.05,\ 1.0,\ 0.95,\ 0.9\,\mathrm{GPa}$.

5.2. Individual interface testing

The proposed interface formulation is first assessed by considering the simple system shown in Fig.(6), where a single interface lies between two prismatic rigid grains, modelled with the boundary element method and meshed with the procedure described in Section 4.1. The edge of the cubic aggregate is $l = 1\,\mu\mathrm{m}$ and the interface lies on the plane $x_3 \equiv z = 0.5\,\mu\mathrm{m}$.

As mentioned, for this specific test, the two grains are assumed as rigid; this is obtained by setting their material constants as $\tilde{c}_{ij} = 10 \times c_{ij}$, with the values c_{ij} given in the previous section. This is done so that the grains may transfer the boundary conditions to the interface as displacements jumps, allowing to investigate the behaviour of the interface without accounting for effects induced by the accumulation of elastic energy. Additionally, maintaining the boundary element representation for the grains, even with this artificially high value of stiffness, allows assessing the correct coupling between boundary element and interface equations. On the other hand, the interface is modelled employing an intrinsic approach, i.e. assuming an initial damage $\omega_0 = 0.01$; all the other interface parameters are collected in Table 1 and have been estimated as detailed in Section 5.1.

Initially, pure mode I and mode II debonding tests under increasing monotonic loading in displacement control are performed. The loads are applied as opening or sliding displacements enforced over the top face of the top grain, at $x_3 = 1\,\mu\mathrm{m}$, while restraining the displacements of the bottom surface. The response of the interface is shown in Fig.(7) in terms of $t_3 = t_3(\delta u_3)$ for mode I and $t_1 = t_1(\delta u_1)$ for mode II. The response of the proposed coupled plastic-damage model is compared to the bilinear response that would be obtained from a pure damage model,

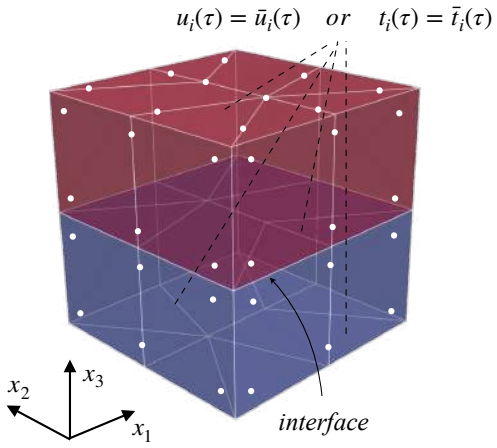

Figure 6: Schematic configuration adopted for testing the proposed cohesive formulation: an individual interface lies between two prismatic quasi-rigid domains modelled with the boundary element method.. The edge of the cubic domain is $l = 1\,\mu\text{m}$. The interface lies on the plane $x_3 = 0.5\,\mu\text{m}$. Both quadrangular and triangular boundary elements appear in the mesh, with their functional nodes represented as bold points.

for which only the damage activation function discussed in Section 3.2 would be considered. For the coupled model, the set of assumed constitutive parameters, especially the values of m and a, induce increments of damage in the elastic-plastic branch so that the interface exhibits softening also without the activation of the specific damage yielding function, i.e. for $\phi_d < 0$. The pure damage activation condition might only be fulfilled, considering e.g. pure mode I loading, if t_n^d would always lie within the endurance surface, in its initial position centred at the origin of the reference frame, that is for a value of pure damage strength less than the endurance surface radius, $t_n^d < r_n$: in this case the interface would exhibit the pure damage bilinear behaviour with softening represented by the dashed curve in Fig.(7).

The discussed monotonic loading cases provide useful information about the quasi-static behaviour of the interface. However, to highlight the novelty and features of the proposed model, which is able to describe damage initiation and evolution under cyclic loading by suitably coupling damage itself with hysteretic plasticity, loading/un-loading/re-loading cyclic loading is considered next. For this purpose, the considered two-grain system is analysed when the top surface is loaded in displacement control, in pure mode I or mode II, with load cycles of increasing amplitude.

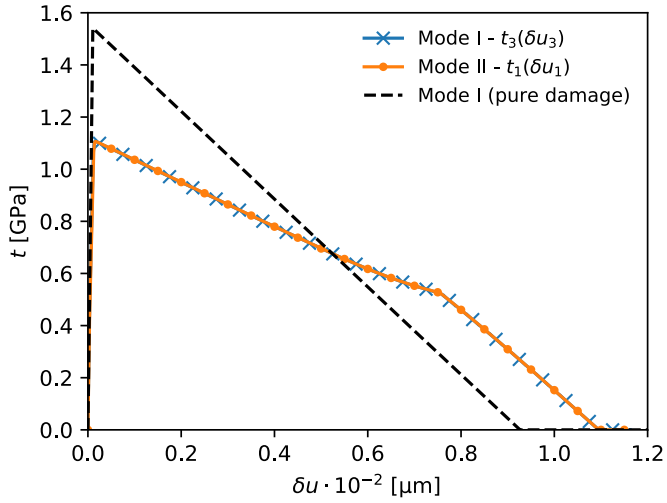

Figure 7: Response of the interface under monotonic increasing loading in displacement control, in pure mode I, $t_3 = t_3(\delta u_3)$, and pure mode II, $t_1 = t_1(\delta u_1)$. The proposed model is compared to the response provided by a pure damage model, obtained by artificially increasing the diameters of the endurance surface.

The cyclic increasing-amplitude mode I loading produces cycles of the normal traction ranging between compressive and tensile values and the response of the interface in terms of normal traction t_3 versus displacement $u_3(\tau)$ enforced on the top surface is reported in Fig.(8), where the hysteretic elastic-plastic behaviour in the un-loading/re-loading cycles can be observed, as well as the pure elastic response in compression states.

The coupled model links hysteretic plasticity with damage evolution and stiffness degradation as the plastic limit condition $\phi_p = 0$ is attained. The hysteretic effect in the coupled model is shown in Fig.(9) for the two-grain system loaded in pure mode I by an amplitude-increasing cyclic displacement u_3 enforced over the top face. In particular, Fig.(9a) shows the evolution of damage versus the value of enforced displacement. Damage increases when the plastic-damage condition $\phi_p = 0$ is attained, mainly during the *loading* branches, although small damage increments also take place during the *un-loading* phase. Fig.(9b) reports the evolution of plastic deformation versus the value of enforced displacement, highlighting positive increments of plastic deformation in the loading and re-loading branches and decrements in the un-loading phases. Decrements of plastic deformation associated to damage increments take place in the un-loading branches when the plastic-damage limit condition ($\phi_p = 0$) is attained and they are governed by the non-associative flow

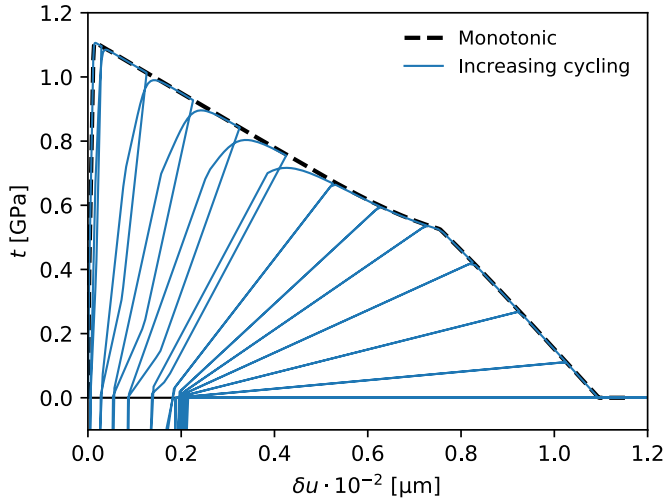

Figure 8: Response of the interface under increasing-amplitude mode I load cycles compared with the response under monotonic opening load.

rules in Eqs.(23). Neither damage nor plastic deformation increments are induced in compression.

The proposed interface model is also tested in pure mode II, simulated by enforcing a displacement u_1 at the top face of the two-grain system. Both the quasi-static and cyclic responses are shown in terms of tangential traction t_1 versus tangential displacement u_1 in Fig.(10), where the hysteresis cycles can be easily observed. Fig.(11) reports the evolution of damage and plastic deformation versus enforced displacement u_1 for increasing-amplitude mode II cycles.

Eventually, the specific features of the coupled model can be discussed by considering the effects on the interface of cyclic loading tractions, whose values are always lower than the interface strength $t_n(\tau) < t_n^{pl}\ \forall\tau$. The low-cycle fatigue tests are performed in load control, by enforcing on the top surface of the two-grains system a tensile *pulsating* traction, i.e. a cyclic tensile traction ranging between zero and a maximum value, $0 \leq t_n(\tau) \leq t_n^{max}$. Four different values of cyclic peak traction are considered: cyclic 1 with $t_n^{max} = 1.05\,\text{GPa} \approx 0.95\,t_n^{pl}$; cyclic 2 with $t_n^{max} = 1.0\,\text{GPa} \approx 0.91\,t_n^{pl}$; cyclic 3 with $t_n^{max} = 0.95\,\text{GPa} \approx 0.86\,t_n^{pl}$; cyclic 4 with $t_n^{max} = 0.9\,\text{GPa} \approx 0.82\,t_n^{pl}$. Fig.(12) shows the interface responses in terms of normal traction t_3 versus normal displacement u_3 for the four differente cyclic loads, comparing them to the response to monotonic increasing load. It is observed that, even when the traction level is always lower than the interface normal strength t_n^{pl}, the interface exhibits plastic accumulation and damage evolution after each load cycle. Fig.(12) also shows how,

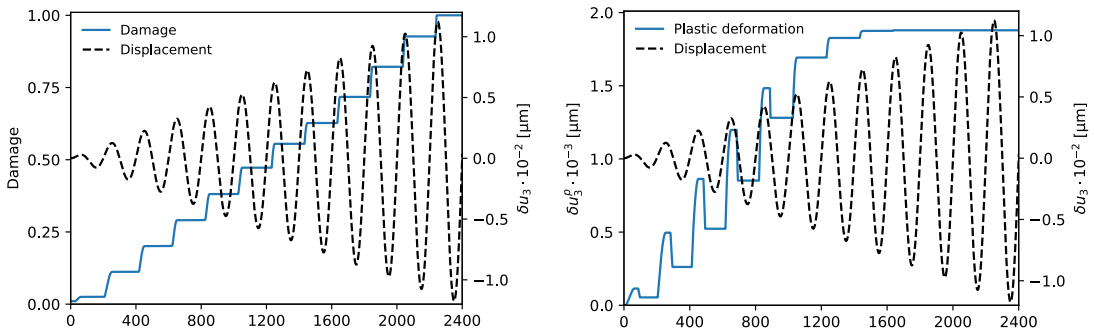

a *b*

Figure 9: Evolution of the interface variables during mode I amplitude-increasing load cycles: *a*) damage; *b*) plastic deformation.

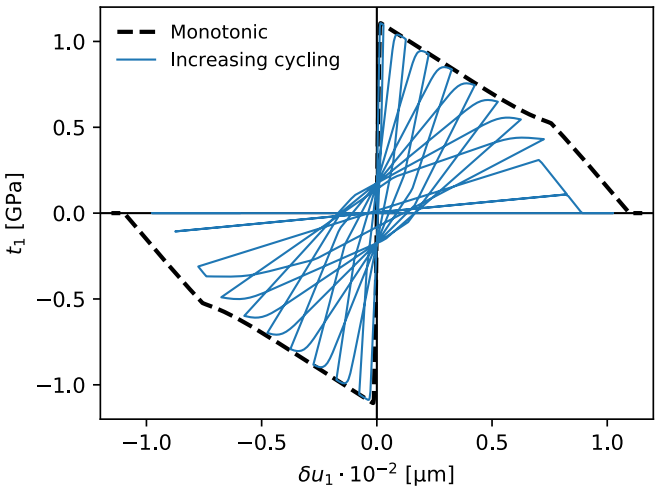

Figure 10: Response of the interface under increasing-amplitude mode II load cycles compared with the response under monotonic sliding load.

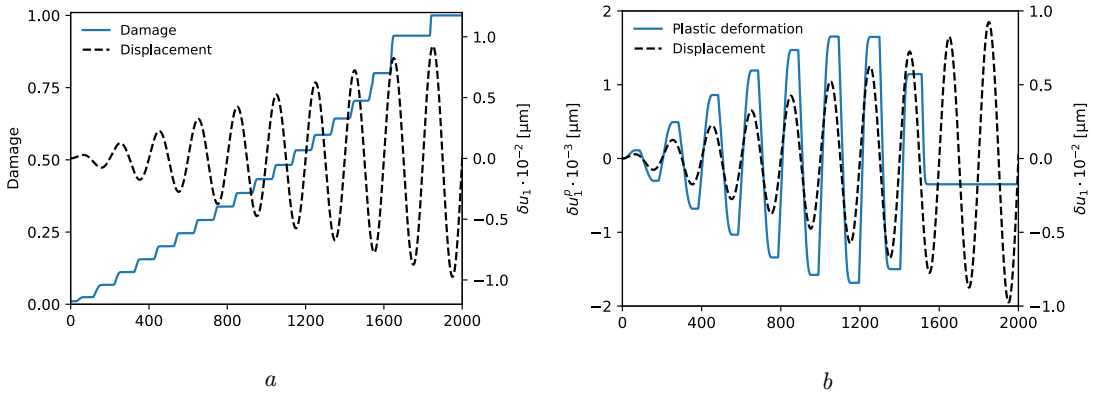

Figure 11: Evolution of the interface variables during mode II amplitude-increasing load cycles: *a*) damage; *b*) plastic deformation.

when the considered cyclic traction-separation curve reaches the monotonic curve, abrupt rupture is triggered. In fact, the analyses are performed in loading control and when the maximum applied traction t_n^{max} becomes greater than the interface *residual* strength, whose envelope is described by the monotonic softening branch, the interface suddenly breaks.

Fig.(13) reports the evolution of damage as a function of the number of loading cycles as well as the interface *fatigue life* versus the stress amplitude $\Delta t_n = t_n^{max}$ for the four mode I tests, confirming the expected dependence of the number of cycles to failure on amplitude of the stress cycle (linear in the logarithmic scale). For the assumed constitutive parameters, the mode II cyclic loading condition produces identical results in terms of number of loading cycles at the debonding condition.

5.3. Polycrystalline aggregates testing

After testing the individual interface, the developed framework is assessed in this section by analysing a few polycrystalline aggregates. Cubic unit cells containing $N_g = 50$ grains are first analysed: these tests illustrate the potential employment of the developed framework in a multiscale perspective, in which the considered unit cells *could* exemplify representative volume elements (RVEs) associated to points of a given macro-continuum. It is underlined that no study of material representativity has been performed here: the tests have been carried out on cubic unit cells with N_g grains without claiming that such number of grains is sufficient for identifying an RVE for the considered material and loading conditions, but only that the framework could be employed in this

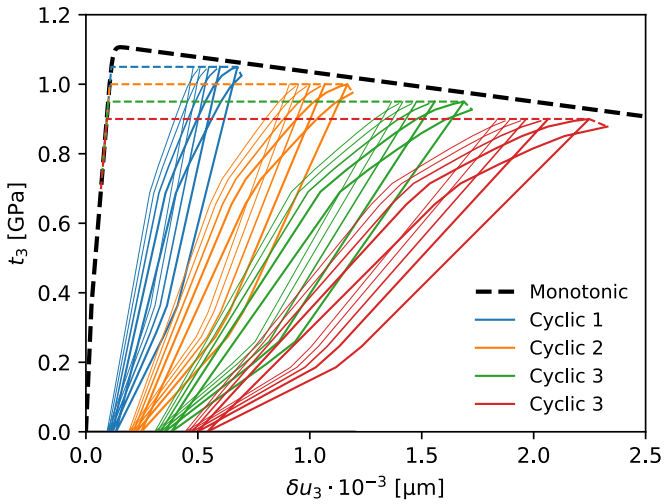

Figure 12: Response of the interface under pure mode I cyclic tractions, for four different values of peak applied normal traction: cyclic 1 with $t_n^{max} \approx 0.95\, t_n^{pl}$; cyclic 2 with $t_n^{max} \approx 0.91\, t_n^{pl}$; cyclic 3 with $t_n^{max} \approx 0.86\, t_n^{pl}$; cyclic 4 with $t_n^{max} \approx 0.82\, t_n^{pl}$.

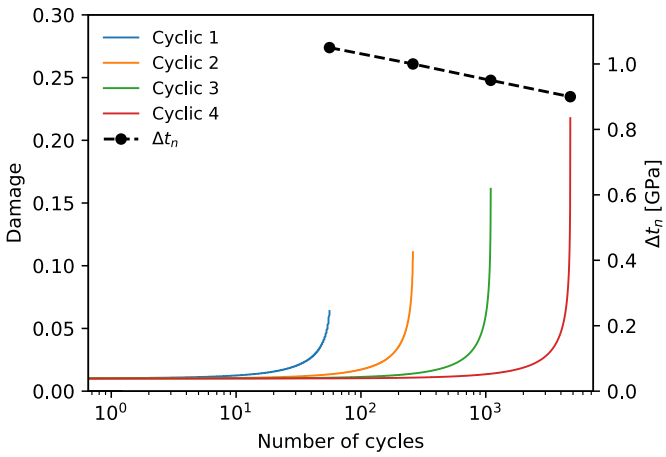

Figure 13: Evolution of damage as a function of the number of cycles (*left axis*) and relationship between load amplitude and number of cycles to failure (*right axis*) for mode I cyclic loading.

sense. Eventually, a pseudo-3D (2D columnar) aggregate is analysed: this last test illustrates the potential use of the framework in the direct analysis of micro-mechanical devices, with well defined geometries, materials, loading and boundary conditions.

All the tests have been performed on individual 36-core nodes of CINECA's Galileo supercomputer (each node contains two 18-cores Intel Xeon E5-2697, v4 – Broadwell – at 2.30 GHz), see `https://www.hpc.cineca.it/hardware/galileo`.

5.3.1. Analysis of fully 3D aggregates

Initially, five different polysilicon aggregates under increasing monotonic loads are investigated, to assess their quasi-static response. Fig.(14) represents the morphology of one of the considered specimens and schematically describes its morphology, mesh and possible boundary conditions. Each of the considered aggregates counts $N_g = 50$ grains of average diameter $d_g = 1.0\,\mu\text{m}$, with random crystallographic orientation in space and contained within a cubic volume whose edge length is $l_{uc} = 2.97\,\mu\text{m}$. The polysilicon constants are given in Section 5.1.

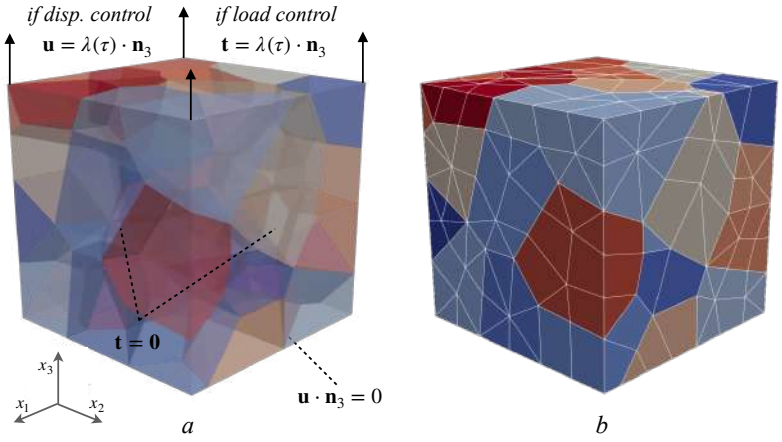

Figure 14: Example morphology for a cubic aggregate containing $N_g = 50$ grains: *a*) schematic of the enforced boundary conditions; *b*) representative mesh.

The aggregates are initially subjected to increasing monotonic tensile load in displacement control up to failure, applied by enforcing the displacements $\bar{\boldsymbol{u}}\,(x_1, x_2, l_{uc}) = \lambda(\tau)\,\boldsymbol{n}_3$ to all the points over the top surface and restraining the points of the bottom surface $\bar{\boldsymbol{u}}\,(x_1, x_2, 0) \cdot \boldsymbol{n}_3 = 0$.

Fig.(15) shows the averaged stress component

$$\Sigma_{33} = \int_V \sigma_{33}\left(\boldsymbol{x}\right) \mathrm{d}V\left(\boldsymbol{x}\right) = \int_{\partial V} t_3 n_3 \, \mathrm{d}\partial V, \tag{45}$$

see e.g. Ref.[21], as a function of the nominal applied strain $\bar{\Gamma}_{33} = 100 \times \bar{\boldsymbol{u}}_3 / l_{uc}$, for the five different morphologies. For the considered grain/interface material constants, the analysed morphologies exhibit brittle behaviour, which is reflected both macroscopically, in the limited extension of the post-peak brach of the stress-strain curves, and microscopically, in the very limited accumulation of intergranular damage up to load levels indefinitely close to the failure load, as shown in Fig.(16), which reports the deformed configuration and the distribution of intergranular damage for the last computed step before failure for three of the five considered morphologies. This is due to the unstable release of the strain elastic energy stored within the grains upon intergranular damage initiation.

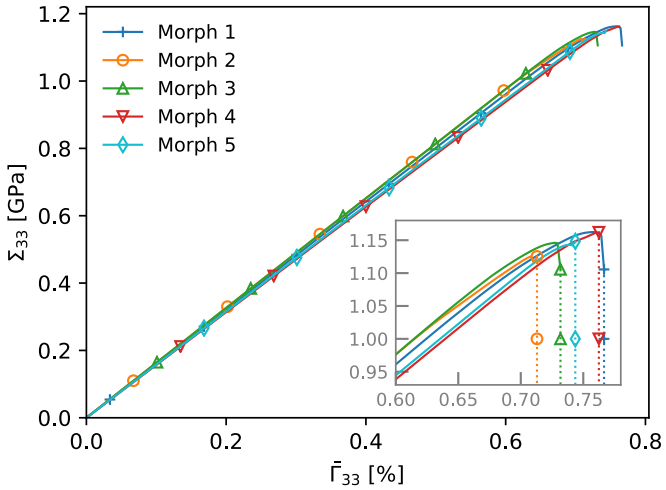

Figure 15: Average stress component σ_{33} versus applied nominal strain $\bar{\Gamma}_{33}$ for the five considered morphologies under increasing monotonic load.

In order to further assess the pure intergranular behaviour under monotonic increasing load, without taking into account the effect of the elastic energy stored in the grains during the loading process, an aggregate of quasi-rigid grains is then considered: analogously to what has been previously done in the test of the individual interface, quasi-rigid grains are simulated by assuming $\tilde{c}_{ij} = 10 \times c_{ij}$, where c_{ij} are the material constants associated to polysilicon. The first of the five

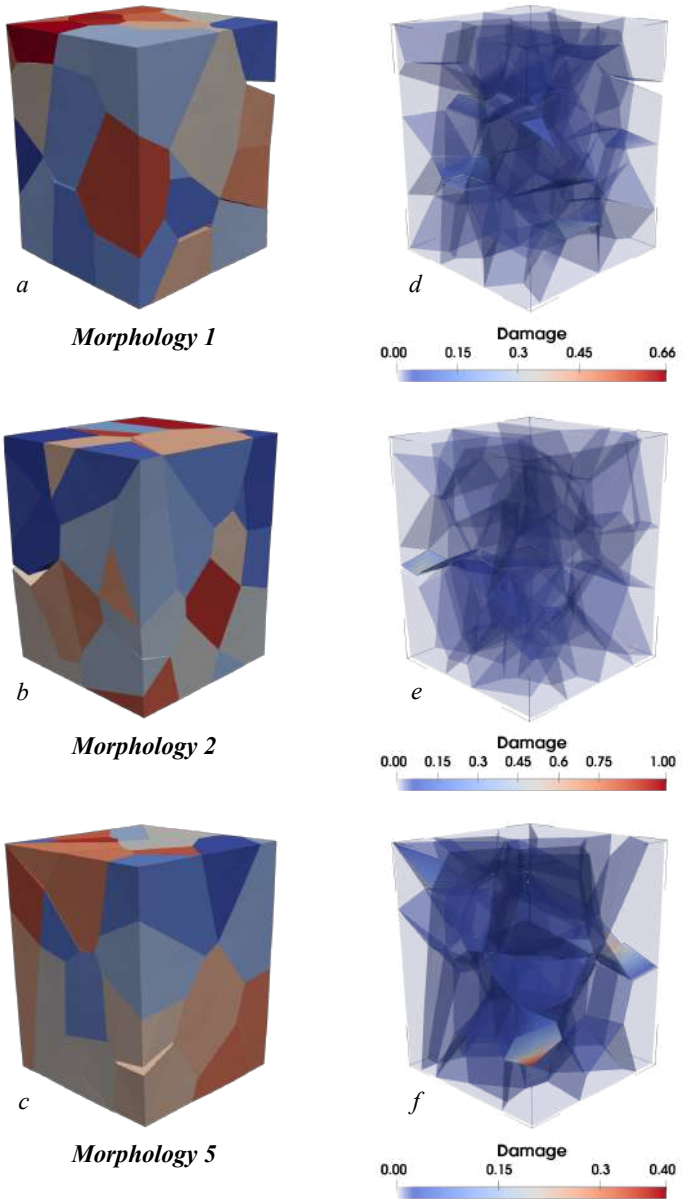

Figure 16: Last computed snapshots for the morphologies 1, 2 and 5, whose averaged stress-strain curves are represented in Fig.(15): deformed configurations (a, b, c) and distribution of intergranular damage (e, f, g). An amplification factor $a_f = 30$ is applied to the computed displacements to obtain the shown deformed configurations.

analysed morphologies is selected and loaded in displacement control, assuming quasi-rigid grains. Fig.(17) reports the curve of the average stress component Σ_{33} versus the nominal strain $\bar{\Gamma}_{33}$: when no elastic energy is stored within the grains, as in the case of quasi-rigid behaviour, all the work of the external loads is fully transferred to the interfaces, which then absorb energy undergoing damage and plasticity evolution in a stable process. Fig.(17) shows as, in this case, the cohesive laws allow tracking the stable evolution of the aggregate up to complete failure. Fig.(18) shows the deformed configuration and the distribution of intergranular damage for the four points A, B, C, D marked in Fig.(17): it may be observed how intergranular damage exhibits a more stable evolution.

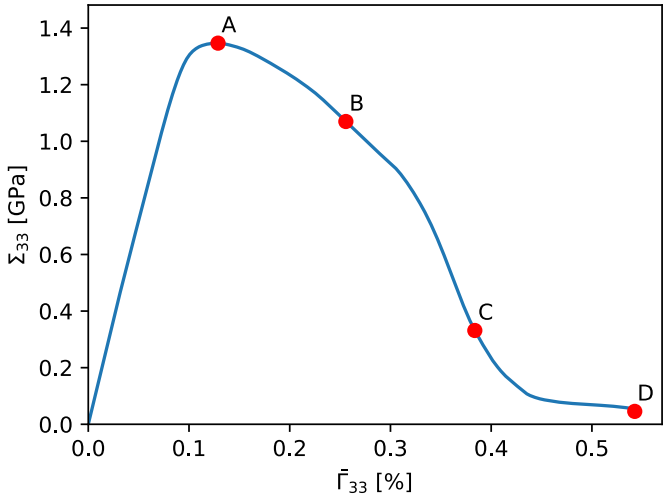

Figure 17: Average stress component Σ_{33} versus applied nominal strain $\bar{\Gamma}_{33}$ for an aggregate of quasi-rigid grains (morphology 1).

Eventually, the evolution of the aggregate under cyclic load is analysed. The first morphology is considered and loaded by restraining the displacements of the bottom surface, $\bar{\boldsymbol{u}}\left(x_1, x_2, 0\right) \cdot \boldsymbol{n}_3 = 0$, and enforcing the traction $\bar{\boldsymbol{t}}\left(x_1, x_2, l_{uc}\right) = \lambda(\tau)\, \boldsymbol{n}_3$ on the top surface, with the loading factor graphically shown in Fig.(19) and defined by

$$\lambda\left(\tau\right) = \frac{\beta\, \bar{t}\,|_{qs}^{max}}{2} \left\{ \frac{4}{T} \left[\tau - \left(\tau - \frac{T}{4} \right) \mathscr{H}\left(\tau - \frac{T}{4} \right) \right] + sin\left(\Xi\, \tau\right) \right\} \qquad \forall \tau > 0, \tag{46}$$

where $\bar{t}\,|_{qs}^{max}$ is the quasi-static failure tensile traction, β is a coefficient using to set the peak load at a fraction of $\bar{t}\,|_{qs}^{max}$, $\mathscr{H}$ is the Heaviside step function and $T = 2\pi/\Xi$. It is worth mentioning that, since no inertial or frequency effects are considered in the formulation, the variable τ appearing

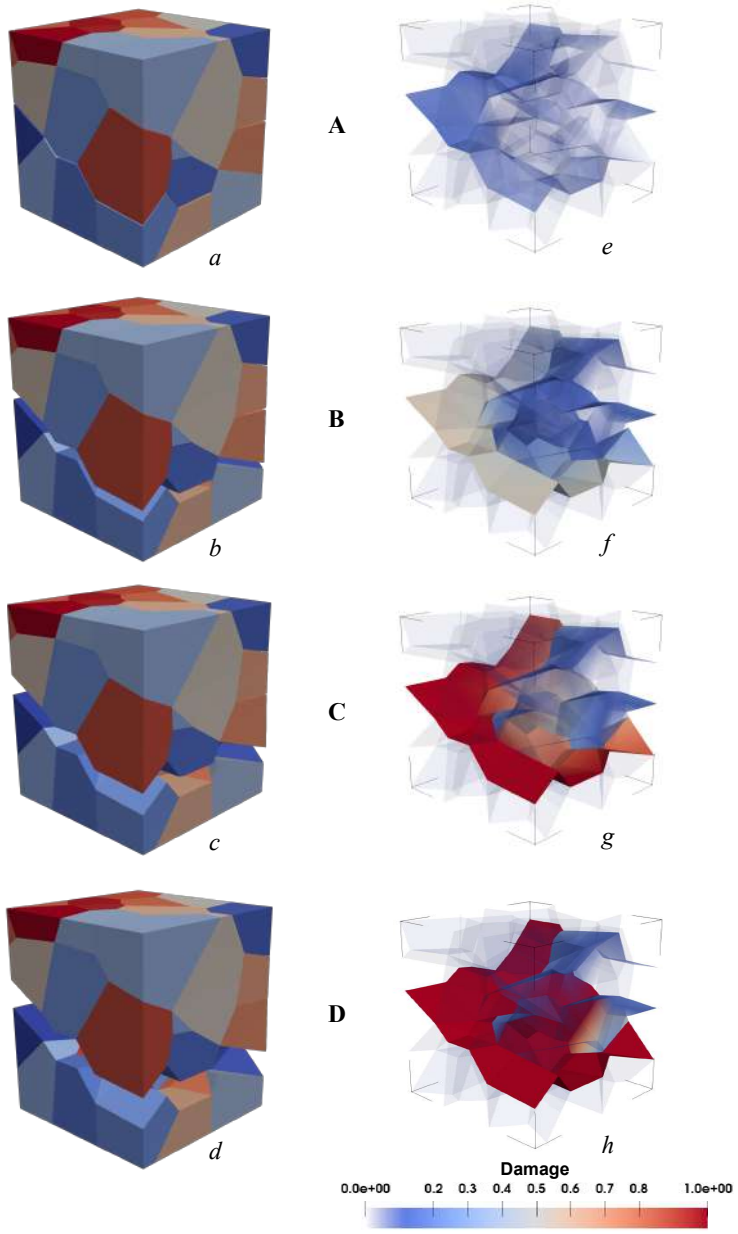

Figure 18: Deformed configurations (a, b, c, d) and distribution of intergranular damage (e, f, g, h) corresponding to the marked points in Fig.(17). An amplification factor $a_f = 30$ is applied to the computed displacements to obtain the shown deformed configurations.

in Eq.(46) is a pseudo-time playing the role of an ordering parameter; analogously the period T and angular frequency Ξ have no real physical or computational role, as the automatic solution step range is automatically set in relation to T. In particular, the pseudo-time step $\Delta\tau$ is selected within the range $\Delta\tau_{min} \leq \Delta\tau \leq \Delta\tau_{max}$, where $\Delta\tau_{max} = T/40$ and $\Delta\tau_{min} = T/4000$. After the successful solution of the system of equations at the pseudo-time step τ_k, the solution at the pseudo-time step $\tau_{k+1} = \tau_k + \Delta\tau_k$ is sought selecting the pseudo-time step increment as $\Delta\tau_k = \Delta\tau_{max} + (\Delta\tau_{min} - \Delta\tau_{max})N^k_{iter}/N^{max}_{iter}$, where N^k_{iter} is the number of iterations to convergence for τ_k and $N^{max}_{iter} = 50$ is the selected maximum number of iterations to convergence, see also Ref.[20].

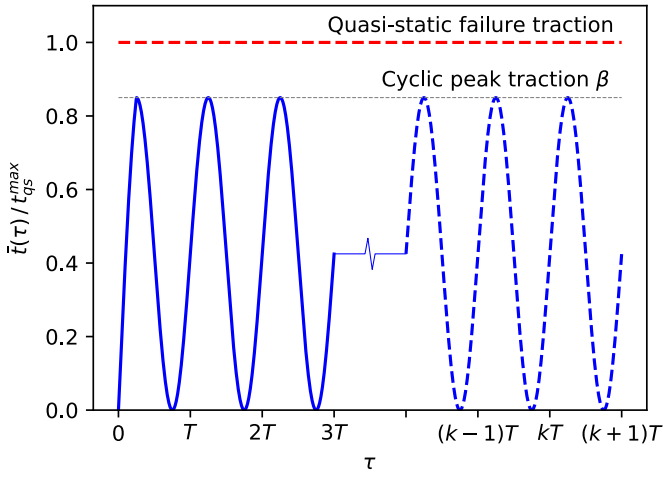

Figure 19: Definition of the loading factor $\lambda(\tau)$.

For the considered morphology, the value of $\bar{t}\,|^{max}_{qs} = \bar{t}_3|^{max}_{qs} = 1.08\,\text{GPa}$ was previously computed running a preliminary quasi-static test in loading control, enforcing a uniform monotonically increasing tensile traction $\bar{\boldsymbol{t}} = \tau\,\boldsymbol{n}_3$ over the aggregate top surface. For $\beta = 0.95$, i.e. when the cycle peak load is at 95% of the quasi-static failure traction, the considered aggregate underwent $N_f = 140$ cycles before failure. Fig.(20) shows the deformed configurations and the intergranular evolution of damage and plastic deformation at the 35-*th*, 70-*th*, 105-*th* and 140-*th* cycle peaks. Also in this case the accumulation of intergranular damage before failure appears to be of modest entity, due to the brittleness of the aggregate.

After considering a cyclic load with peak values at 95% of the quasi-static failure traction, $\beta = 0.95$ in Eq.(46), also cyclic loads with peak loads at 90% and 87.5% of the quasi-static failure

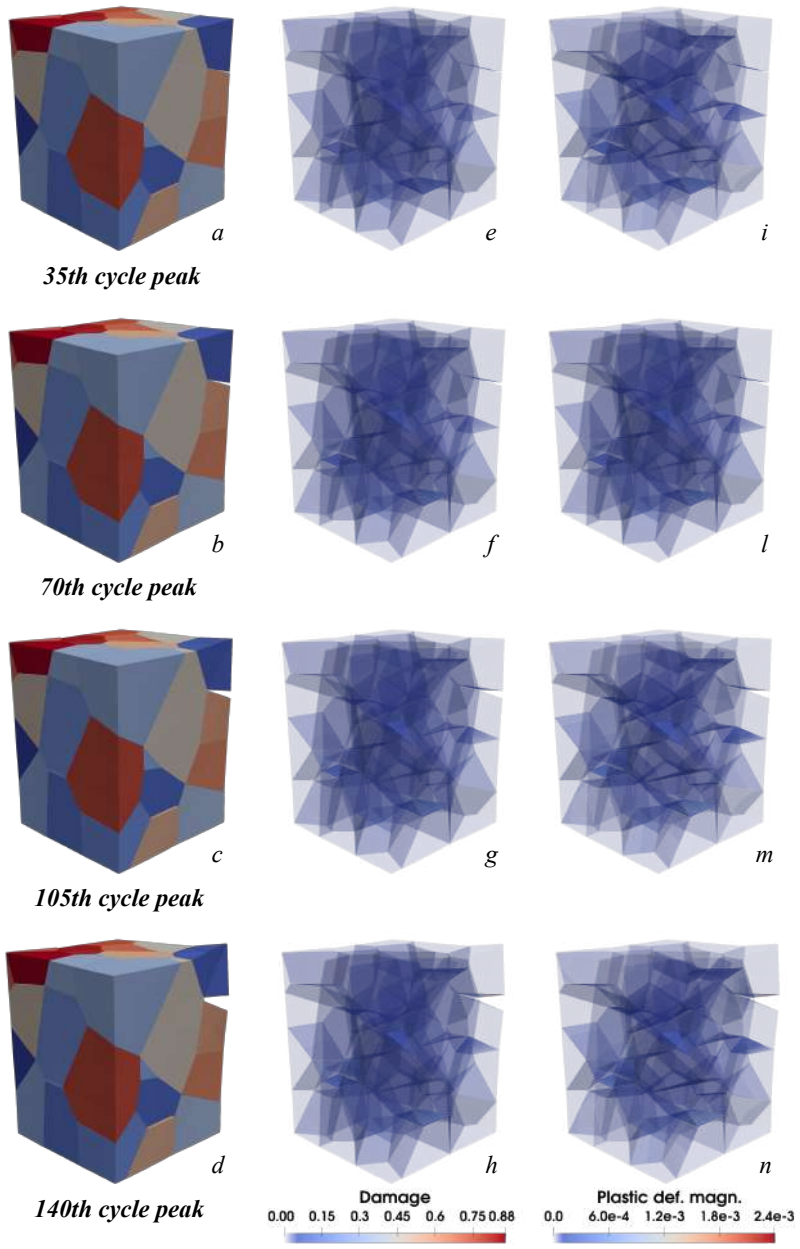

Figure 20: Deformed configuration (a, b, c, d), intergranular distribution of damage (e, f, g, h) and plastic deformation (i, l, m, n) at different peak loads for the analysed morphology ($\beta = 0.95$, $N_c = 140$).

traction have been considered, $\beta = \{0.90, 0.875\}$. For $\beta = 0.90$ the number of cycles to failure was $N_c = 1380$, while for $\beta = 0.875$ the computation of N_c was not completed in the allocated wall time (23 h) on the employed HPC system (1813 full cycles were however completed before the job was killed by the system). Since the number of cycles to failure for the considered morphology was computed only for 2 load levels, the fatigue life curve is not reported (a fatigue life curve will be shown in the next section for a pseudo-3D aggregate).

Eventually, it may be of interest to mention that, on the HPC machines specified above (CINECA's Galileo), for $\beta = 0.95$, $N_c = 140$ cycles were computed in 1 h 50 min, for $\beta = 0.90$, $N_c = 1380$ cycles were computed in 10 h 28 min, while for $\beta = 0.875$, 1813 cycles were computed in 23 h. The information on computing times is given for informative purposes, as no systematic assessment of the computing performance of the implemented framework has been performed.

5.3.2. Pseudo-3D bracket

The present test considers the specimen shown in Fig.(21), where the geometry, tessellation, mesh and boundary conditions are schematically represented. The bracket size is defined by $H = 19.8\,\mu\text{m}$, $W = 0.4\,H$, $h = 0.1\,H$, $w = 0.25\,W$, and thickness $T = 0.05\,H$, considering that the curved walls are parabolic, and it has been determined so that the each grain has average diameter $d_g = 1.0\,\mu\text{m}$ in the x_1x_2 plane. The tessellation has been generated by extruding a 2D tessellation along the x_3 axis, so to obtain a 2D columnar, or pseudo-3D, morphology, and it comprises $N_g = 151$ grains with random crystallographic orientation in the 3D space. The concave external boundaries have been obtained by using the clipping tools available in version `4.1` of `Neper` (`http://neper.sourceforge.net`) [12].

The bracket is clamped at the bottom end, $\bar{\boldsymbol{u}}(x_1, 0, x_3) = \boldsymbol{0}$, and loaded by a uniform cyclic tensile traction $\bar{\boldsymbol{t}}(x_1, H, x_3) = \lambda(\tau)\,\boldsymbol{n}_2$ applied over the other end, so to deliver a repeated tensile loading. The loading factor $\lambda(\tau)$ is still specified by Fig.(19) and Eq.(46), where $\bar{t}\,|_{qs}^{max} = \bar{t}_2|_{qs}^{max} = 0.52\,\text{GPa}$ was preliminarily determined by performing a quasi-static monotonic loading test in load control.

In the first test, the bracket has been subjected to a repeated tensile load with peaks at 95% of the quasi-static failure load, $\beta = 0.95$ in Eq.(46). In this condition, the bracket underwent $N_c = 63$ cycles and Fig.(22) shows the deformed configuration and intergranular distribution of damage and plastic deformation at the last computed peak before failure. Also in this case, the

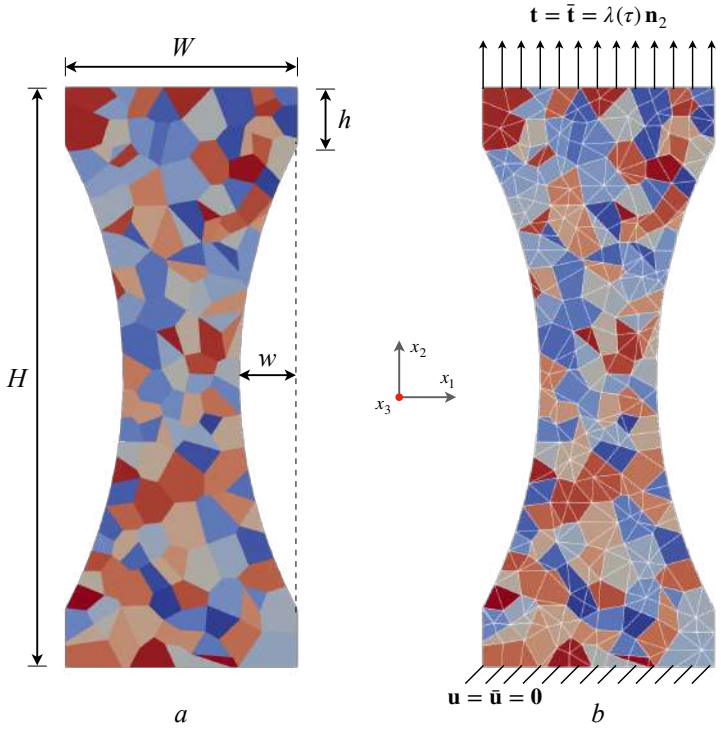

Figure 21: Schematic representation of the analysed pseudo-3D polycrystalline aggregate: *a*) geometry and size; *b*) mesh and boundary conditions.

failure process shows the hallmarks of brittleness, with very limited accumulation of damage up to the step immediately preceding the abrupt failure, accompanied by the release of the elastic strain energy stored within the grains in the deformation process.

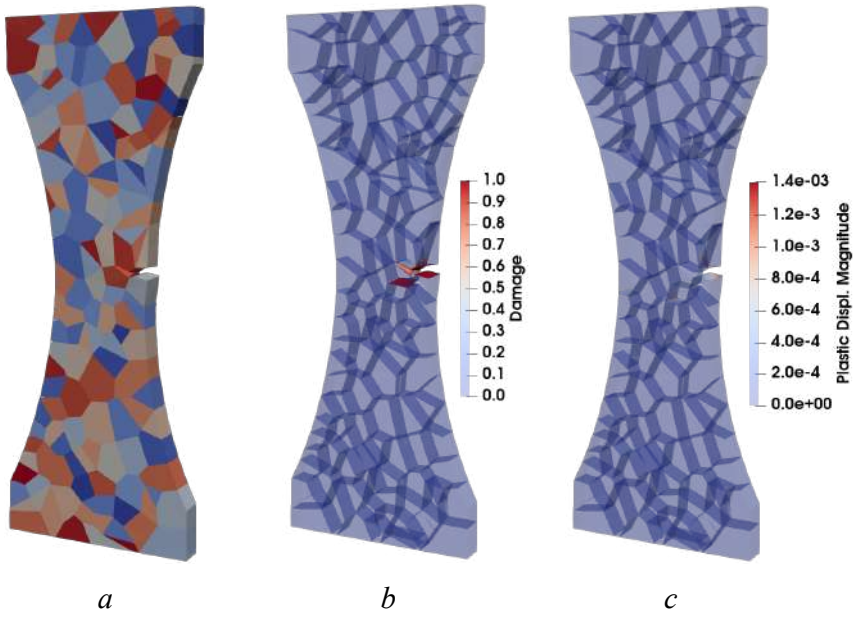

Figure 22: Snapshot at the last (63-*th*) load peak for the analysed pseudo-3D aggregate, loaded by an alternated traction with $\beta = 0.95$: *a*) deformed configuration; *b*) distribution of intergranular damage; *c*) distribution of intergranular plastic deformation. An amplification factor $a_f = 10$ is applied to the computed displacements to obtain the shown deformed configuration.

After the cyclic repeated load at $\beta = 0.95$, also the cases $\beta = \{0.90, 0.875, 0.85\}$ have been analysed and it has been found that the bracket underwent, respectively, $N_c = \{354, 759, 1750\}$ cycles before failure. The corresponding fatigue life curve has been reported in Fig.(23), where it can be noted the liner trend when N_c is reported in a logarithmic scale.

Fig.(23) also reports an indication of the computational times required by the various tests on the employed HPC system. It is reiterated that this information is reported only for informative purposes and should not be considered as a systematic assessment of the framework performances: it is noted, for example, that the computation of $N_c = 759$ cycles for $\beta = 0.875$ requires only few minutes more that the computation of $N_c = 354$ cycles for $\beta = 0.90$, probably due to the fact that the first case the disk record of the microstructural state has been required once every 1000 solution

steps, instead than at every step, as done for $\beta = 0.90$, which motivates the little difference in CPU time.

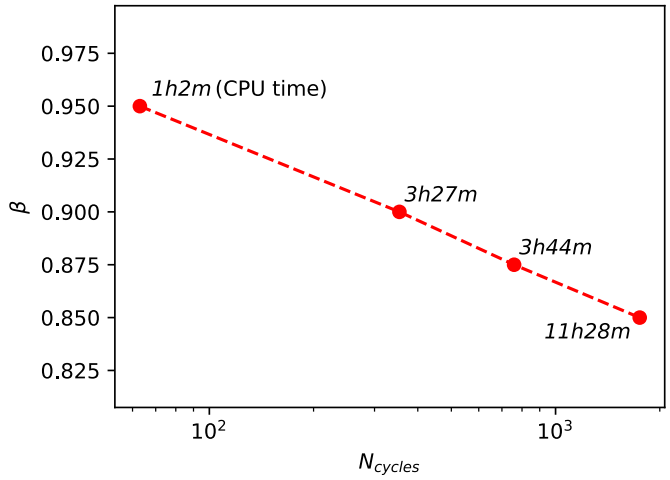

Figure 23: Fatigue life versus β for the considered pseudo-3D bracket under tensile alternate load. The annotations also reports the computing time in the employed HPC system.

6. Discussion and further developments

In this work, a novel framework for the analysis of polycrystalline aggregates under cyclic loading has been proposed, developed, implemented and computationally assessed. The tool is based on a three-dimensional multi-region boundary element formulation enriched with intergranular cohesive laws coupling damage and plasticity in a thermodynamically consistent approach. The intergranular laws are able to track the initiation of damage and either its evolution under quasi-static monotonically increasing loading or its cycle-by-cycle accumulation up to interface failure. The results presented and discussed have shown the potential of the framework for multiscale materials modelling as well as for computational micromechanics and analysis and design of micro-mechanical systems.

Few considerations about the scope, limitations and further developments are worthwhile. First of all, it must be highlighted that the framework, in its present implementation, is suitable for modelling materials in which non-linear processes, namely plasticity and/or damage initiation and

evolution, are highly confined within the intergranular regions. An example is provided by polysilicon, e.g. polycrystalline silicon, one of the materials most employed in the manufacturing of MEMS [73], for which some authors have proposed the existence of thin *amorphous* grain-boundary regions exhibiting non-traditional forms of plastic deformation [34].

However, in general, low-cycle damage and failure emerge from the interaction of several complex micro-mechanisms [36]. Low cycle fatigue in materials exhibiting crystal plasticity, e.g. nickel-base alloys, is often initiated by the localisation of plastic slip, under cyclic loading, at persistent slip bands, which then evolve in low-cycle crack initiation sites [79]. In its present implementation, the proposed model is not able to represent such complex phenomena. To investigate and capture such processes, the framework should be enriched with the capability of modelling crystal plasticity and transgranular cracking: both mechanisms have been separately modelled within the scope of the present grain-boundary formulation [80, 22], but their integration within the present low-cycle modelling strategy represents a non-trivial task, both from the theoretical and computational points of view, and could form the object of further investigation. Another limitation of the formulation is related to the lack of consideration of *rate-dependent* effects, which may occur in general loading cases [81]. Indeed, the proposed cohesive laws have been developed in a rate-independent framework: the inclusion of rate-dependency in the plasticity/damage evolution laws could noticeably extend the model capability.

The developed framework provides a tool for the qualitative study of materials whose behaviour can be framed within the identified scope. To enhance its quantitive predictive capability, the parameters entering the formulation should be calibrated, either experimentally or resorting to computational tools addressing the material mechanics at lower scales. In Section 5.1, some heuristic estimates of the model parameters have been discussed. However, the experimental calibration of the proposed framework is an issue deserving systematic assessment and focused investigation.

An interesting direction of further research could be related to the extension of the present boundary element framework through hybridization with other numerical techniques: the conjoined employment of BEM and the rapidly emerging *virtual element method* [82] could extend the scope and capability of the framework in a multi-technique optimization perspective [83, 84, 85, 86].

Eventually, the performed tests have highlighted the need of large amounts of storage memory for the solution of the systems of equations produced by the present formulation, which is here tackled employing the third party solver `PARDISO` (`https://www.pardiso-project.org`). This

aspect, which could induce potential issues when addressing large aggregates, could be tackled tailoring specific iterative solvers in conjunction with special matrix formats, namely fast multipoles [68] and hierarchical matrices [69, 70, 87, 88], to the analysis of the multi-region polycrystalline problem. This challenging investigative effort could result in a highly effective and more competitive computational tool for materials micro-mechanics and for the design and analysis of MEMS.

7. Conclusions

In this work a three-dimensional model for the analysis of polycrystalline aggregates undergoing low-cycle degradation up to complete failure has been developed. The model is based on the conjoined use of a three-dimensional Voronoi multi-region boundary element formulation for polycrystalline aggregates and of thermo-dynamically consistent cohesive laws, coupling plasticity and damage, for tracking the accumulation of intergranular damage under the action of cyclic loads. The proposed cohesive laws has been implemented and tested on individual interfaces and the complete framework has then been assessed by simulating the behaviour of a few 3D and psudo-3D aggregates. The obtained results confirm the potential of the methodology for multiscale materials modelling and for the analysis and design of micro-devices, e.g. MEMS, also highlighting directions of further investigation.

Acknowledgements

I.B. acknowledges the support of the Italian Ministry of Education, University and Research through the project DEVISU, funded under the scheme PRIN-2107 (Grant 22017ZX9X4K_006). The authors acknowledge the support of CINECA's Italian Centre for Super Computing Applications and Innovation staff for the access and use of their HPC infrastructure, `http://www.hpc.cineca.it`. The authors thank Prof. Romain Quey of the École des Mines de Saint-Étienne, France, for his support in the use of `Neper`, `https://neper.info/#`.

References

[1] E. B. Tadmor, R. E. Miller, Modeling materials: continuum, atomistic and multiscale techniques, Cambridge University Press, 2011.

[2] B. C. Kim, P. M. Weaver, K. Potter, Manufacturing characteristics of the continuous tow shearing method for manufacturing of variable angle tow composites, Composites Part A: Applied Science and Manufacturing 61 (2014) 141–151. doi:https://doi.org/10.1016/j.compositesa.2014.02.019.
URL https://www.sciencedirect.com/science/article/pii/S1359835X14000712

[3] N. Maluf, K. Williams, An introduction to microelectromechanical systems engineering, Artech House, 2004.

[4] P. R. Budarapu, X. Zhuang, T. Rabczuk, S. P. Bordas, Chapter one - multiscale modeling of material failure: Theory and computational methods, in: M. I. Hussein (Ed.), Advances in Crystals and Elastic Metamaterials, Part 2, Vol. 52 of Advances in Applied Mechanics, Elsevier, 2019, pp. 1–103. doi:https://doi.org/10.1016/bs.aams.2019.04.002.
URL https://www.sciencedirect.com/science/article/pii/S006521561930002X

[5] A. King, G. Johnson, D. Engelberg, W. Ludwig, J. Marrow, Observations of intergranular stress corrosion cracking in a grain-mapped polycrystal, Science 321 (5887) (2008) 382–385.

[6] A. Lyckegaard, E. M. Lauridsen, W. Ludwig, R. W. Fonda, H. F. Poulsen, On the use of laguerre tessellations for representations of 3d grain structures, Advanced Engineering Materials 13 (3) (2011) 165–170. doi:10.1002/adem.201000258.
URL http://dx.doi.org/10.1002/adem.201000258

[7] F. Fritzen, T. Böhlke, E. Schnack, Periodic three-dimensional mesh generation for crystalline aggregates based on voronoi tessellations, Computational Mechanics 43 (5) (2009) 701–713. doi:10.1007/s00466-008-0339-2.
URL https://doi.org/10.1007/s00466-008-0339-2

[8] I. Simonovski, L. Cizelj, Automatic parallel generation of finite element meshes for complex spatial structures, Computational Materials Science 50 (5) (2011) 1606 – 1618. doi:https://doi.org/10.1016/j.commatsci.2010.12.014.
URL http://www.sciencedirect.com/science/article/pii/S0927025610006713

[9] T. Luther, C. KÃűnke, Polycrystal models for the analysis of intergranular crack growth in metallic materials, Engineering Fracture Mechanics 76 (15) (2009) 2332 – 2343. doi:https:

//doi.org/10.1016/j.engfracmech.2009.07.006.
URL http://www.sciencedirect.com/science/article/pii/S0013794409002185

[10] H. D. Espinosa, P. D. Zavattieri, A grain level model for the study of failure initiation and evolution in polycrystalline brittle materials. part i: Theory and numerical implementation, Mechanics of Materials 35 (3) (2003) 333–364.

[11] I. Simonovski, L. Cizelj, Cohesive zone modeling of intergranular cracking in polycrystalline aggregates, Nuclear Engineering and Design 283 (2015) 139 – 147, sI:NENE 2013. doi:https://doi.org/10.1016/j.nucengdes.2014.09.041.
URL http://www.sciencedirect.com/science/article/pii/S0029549314005548

[12] R. Quey, P. R. Dawson, F. Barbe, Large scale 3D random polycrystals for the finite element method: Generation, meshing and remeshing, Computer Methods in Applied Mechanics and Engineering 200 (2011) 1729–1745.

[13] R. Quey, L. Renversade, Optimal polyhedral description of 3d polycrystals: Method and application to statistical and synchrotron x-ray diffraction data, Computer Methods in Applied Mechanics and Engineering 330 (Supplement C) (2018) 308 – 333. doi:https://doi.org/10.1016/j.cma.2017.10.029.
URL http://www.sciencedirect.com/science/article/pii/S0045782517307028

[14] P. Banerjee, The boundary element methods in engineering, McGraw-Hill, 1994, (pp. 177–188).

[15] M. H. Aliabadi, The boundary element method: applications in solids and structures., Vol. 2, John Wiley & Sons Ltd, England, 2002.

[16] G. Sfantos, M. Aliabadi, A boundary cohesive grain element formulation for modelling intergranular microfracture in polycrystalline brittle materials, International journal for numerical methods in engineering 69 (8) (2007) 1590–1626. doi:10.1002/nme.1831.

[17] A. Galvis, P. Sollero, 2d analysis of intergranular dynamic crack propagation in polycrystalline materials a multiscale cohesive zone model and dual reciprocity boundary elements, Computers & Structures 164 (2016) 1 – 14. doi:https://doi.org/10.1016/j.compstruc.2015.11.004.
URL http://www.sciencedirect.com/science/article/pii/S0045794915003016

[18] G. Geraci, M. Aliabadi, Micromechanical boundary element modelling of transgranular and intergranular cohesive cracking in polycrystalline materials, Engineering Fracture Mechanics 176 (2017) 351–374.

[19] G. Geraci, M. H. Aliabadi, Micromechanical modeling of cohesive thermoelastic steady-state and transient cracking in polycrystalline materials, International Journal for Numerical Methods in Engineering 117 (12) (2019) 1205–1233. arXiv:https://onlinelibrary.wiley.com/doi/pdf/10.1002/nme.5997, doi:10.1002/nme.5997.
URL https://onlinelibrary.wiley.com/doi/abs/10.1002/nme.5997

[20] I. Benedetti, M. Aliabadi, A three-dimensional cohesive-frictional grain-boundary micromechanical model for intergranular degradation and failure in polycrystalline materials, Computer Methods in Applied Mechanics and Engineering 265 (2013) 36–62. doi:10.1016/j.cma.2013.05.023.

[21] V. Gulizzi, A. Milazzo, I. Benedetti, An enhanced grain-boundary framework for computational homogenization and micro-cracking simulations of polycrystalline materials, Computational Mechanics 56 (4) (2015) 631–651. doi:10.1007/s00466-015-1192-8.

[22] V. Gulizzi, C. Rycroft, I. Benedetti, Modelling intergranular and transgranular micro-cracking in polycrystalline materials, Computer Methods in Applied Mechanics and Engineering 329 (2018) 168 – 194. doi:https://doi.org/10.1016/j.cma.2017.10.005.
URL http://www.sciencedirect.com/science/article/pii/S0045782517306746

[23] A. F. Galvis, R. Q. RodrÃŋguez, P. Sollero, Analysis of three-dimensional hexagonal and cubic polycrystals using the boundary element method, Mechanics of Materials 117 (2018) 58–72. doi:https://doi.org/10.1016/j.mechmat.2017.10.009.
URL https://www.sciencedirect.com/science/article/pii/S016766361730337X

[24] I. Benedetti, V. Gulizzi, A. Milazzo, A microstructural model for homogenisation and cracking of piezoelectric polycrystals, Computer Methods in Applied Mechanics and Engineering 357 (2019) 112595. doi:https://doi.org/10.1016/j.cma.2019.112595.
URL http://www.sciencedirect.com/science/article/pii/S0045782519304712

[25] A. F. Galvis, P. A. Santos-FlÃşrez, P. Sollero, M. de Koning, L. C. Wrobel, Multiscale model of the role of grain boundary structures in the dynamic intergranular failure of polycrystal

aggregates, Computer Methods in Applied Mechanics and Engineering 362 (2020) 112868. doi:https://doi.org/10.1016/j.cma.2020.112868.
URL https://www.sciencedirect.com/science/article/pii/S0045782520300499

[26] I. Benedetti, V. Gulizzi, A. Milazzo, Grain-boundary modelling of hydrogen assisted intergranular stress corrosion cracking, Mechanics of Materials 117 (2018) 137–151. doi:10.1016/j.mechmat.2017.11.001.
URL https://www.scopus.com/inward/record.uri?eid=2-s2.0-85037155275&doi=10.1016%2fj.mechmat.2017.11.001&partnerID=40&md5=38ef17b25776893b9871f8378ae3d731

[27] G. Sfantos, M. Aliabadi, Multi-scale boundary element modelling of material degradation and fracture, Computer Methods in Applied Mechanics and Engineering 196 (7) (2007) 1310–1329. doi:10.1016/j.cma.2006.09.004.

[28] J. E. Alvarez, A. F. Galvis, P. Sollero, Multiscale dynamic transition of 2d metallic materials using the boundary element method, Computational Materials Science 155 (2018) 383–392. doi:https://doi.org/10.1016/j.commatsci.2018.09.002.
URL https://www.sciencedirect.com/science/article/pii/S0927025618305962

[29] I. Benedetti, M. Aliabadi, Multiscale modeling of polycrystalline materials: A boundary element approach to material degradation and fracture, Computer Methods in Applied Mechanics and Engineering 289 (2015) 429 – 453. doi:http://dx.doi.org/10.1016/j.cma.2015.02.018.

[30] I. Benedetti, V. Gulizzi, A grain-scale model for high-cycle fatigue degradation in polycrystalline materials, International Journal of Fatigue 116 (2018) 90 – 105. doi:https://doi.org/10.1016/j.ijfatigue.2018.06.010.
URL http://www.sciencedirect.com/science/article/pii/S0142112318302287

[31] O. Nguyen, E. Repetto, M. Ortiz, R. Radovitzky, A cohesive model of fatigue crack growth, International Journal of Fracture 110 (4) (2001) 351–369. doi:10.1023/A:1010839522926.
URL https://doi.org/10.1023/A:1010839522926

[32] K. Roe, T. Siegmund, An irreversible cohesive zone model for interface fatigue crack growth simulation, Engineering Fracture Mechanics 70 (2) (2003) 209 – 232. doi:https://doi.org/

10.1016/S0013-7944(02)00034-6.
URL http://www.sciencedirect.com/science/article/pii/S0013794402000346

[33] Q. Yu, J. Zhang, Y. Jiang, Fatigue damage development in pure polycrystalline magnesium under cyclic tension-compression loading, Materials Science and Engineering: A 528 (25) (2011) 7816 – 7826. doi:https://doi.org/10.1016/j.msea.2011.06.064.
URL http://www.sciencedirect.com/science/article/pii/S0921509311007313

[34] H. Kahn, L. Chen, R. Ballarini, A. Heuer, Mechanical fatigue of polysilicon: Effects of mean stress and stress amplitude, Acta Materialia 54 (3) (2006) 667 – 678. doi:https://doi.org/10.1016/j.actamat.2005.10.007.
URL http://www.sciencedirect.com/science/article/pii/S1359645405005902

[35] W. M. van Spengen, Static crack growth and fatigue modeling for silicon mems, Sensors and Actuators A: Physical 183 (2012) 57 – 68. doi:https://doi.org/10.1016/j.sna.2012.05.042.
URL http://www.sciencedirect.com/science/article/pii/S0924424712003639

[36] P. Zhang, S. Qu, Q. Duan, S. Wu, S. Li, Z. Wang, Z. Zhang, Low-cycle fatigue-cracking mechanisms in fcc crystalline materials, Philosophical Magazine 91 (2) (2011) 229–249. arXiv:https://doi.org/10.1080/14786435.2010.518169, doi:10.1080/14786435.2010.518169.
URL https://doi.org/10.1080/14786435.2010.518169

[37] C. H. Rycroft, Voro++: A three-dimensional Voronoi cell library in C++, Chaos 19 (2009) 041111.

[38] J. Bomidi, N. Weinzapfel, F. Sadeghi, Three-dimensional modelling of intergranular fatigue failure of fine grain polycrystalline metallic mems devices, Fatigue & Fracture of Engineering Materials & Structures 35 (11) (2012) 1007–1021.

[39] A. Corigliano, O. Allix, Some aspects of interlaminar degradation in composites, Comp. Meth. Appl. Mech. Eng. 185 (2-4) (2000) 203–224.

[40] A. Spada, G. Giambanco, P. Rizzo, Damage and plasticity at the interfaces in composite materials and structures, Comp. Meth. Appl. Mech. Eng. 198 (49-52) (2009) 3884–3901.

[41] G. Alfano, M. Crisfield, Finite element interface models for the delamination analysis of laminated composites: Mechanical and computational issues, Int. J. Num. Meth. Eng. 50 (7) (2001) 1701–1736.

[42] F. Parrinello, G. Marannano, G. Borino, A thermodynamically consistent cohesive-frictional interface model for mixed mode delamination, Engineering Fracture Mechanics 153 (2016) 61–79. doi:10.1016/j.engfracmech.2015.12.001.

[43] F. Parrinello, G. Borino, Non associative damage interface model for mixed mode delamination and frictional contact, European Journal of Mechanics / A Solids 76 (2019) 108–122.

[44] F. Parrinello, B. Failla, G. Borino, Cohesive-frictional interface constitutive model, Int. J. Solids Structures 46 (13) (2009) 2680–2692.

[45] J. Mosler, I. Scheider, A thermodynamically and variationally consistent class of damage-type cohesive models, J. Mech. Physics Solids 59 (8) (2011) 1647–1668.

[46] I. Guiamatsia, G. Nguyen, A thermodynamics-based cohesive model for interface debonding and friction, Int. J. Solids Structures 51 (3-4) (2014) 647–659.

[47] R. Serpieri, E. Sacco, G. Alfano, A thermodynamically consistent derivation of a frictional-damage cohesive-zone model with different mode i and mode ii fracture energies, Eur. J. Mech., A/Solids 49 (2015) 13–25.

[48] F. Parrinello, G. Borino, Integration of finite displacement interface element in reference and current configurations, Meccanica 53 (6) (2018) 1455–1468.

[49] A. Needleman, An analysis of decohesion along an imperfect interface, International Journal of Fracture 42 (1) (1990) 21–40. doi:10.1007/BF00018611.

[50] Q. Yang, D. Shim, S. Spearing, A cohesive zone model for low cycle fatigue life prediction of solder joints, Microelectronic Engineering 75 (1) (2004) 85–95. doi:10.1016/j.mee.2003.11.009.

[51] S. Oller, O. Salomón, E. OÃśate, A continuum mechanics model for mechanical fatigue analysis, Computational Materials Science 32 (2) (2005) 175–195. doi:10.1016/j.commatsci.2004.08.001.

[52] X. Martinez, S. Oller, L. Barbu, A. Barbat, A. de Jesus, Analysis of ultra low cycle fatigue problems with the barcelona plastic damage model and a new isotropic hardening law, International Journal of Fatigue 73 (2015) 132 – 142. doi:https://doi.org/10.1016/j.ijfatigue.2014.11.013.
URL http://www.sciencedirect.com/science/article/pii/S0142112314003016

[53] P. Carrara, L. D. Lorenzis, A coupled damage-plasticity model for the cyclic behavior of shear-loaded interfaces, Journal of the Mechanics and Physics of Solids 85 (2015) 33 – 53. doi:https://doi.org/10.1016/j.jmps.2015.09.002.

[54] P. Carrara, M. Ambati, R. Alessi, L. D. Lorenzis, A framework to model the fatigue behavior of brittle materials based on a variational phase-field approach, Computer Methods in Applied Mechanics and Engineering (2019) 112731doi:https://doi.org/10.1016/j.cma.2019.112731.

[55] R. H. J. Peerlings, W. A. M. Brekelmans, R. de Borst, M. G. D. Geers, Gradient-enhanced damage modelling of high-cycle fatigue, International Journal for Numerical Methods in Engineering 49 (12) (2000) 1547–1569. doi:10.1002/1097-0207(20001230)49:12<1547::AID-NME16>3.0.CO;2-D.
URL http://dx.doi.org/10.1002/1097-0207(20001230)49:12<1547::AID-NME16>3.0.CO;2-D

[56] B. Coleman, W. Noll, The thermodynamics of elastic materials with heat conduction and viscosity, Arch. Rat. Mech. Analysis 13 (1963) 167–178.

[57] A. Corigliano, Formulation, identification and use of interface models in the numerical analysis of composite delamination, Int. J. Solids Structures 30 (20) (1993) 2779–2811.

[58] L. Daudeville, O. Allix, P. Ladevéze, Delamination analysis by damage mechanics: Some applications, Comp. Engng 5 (1) (1995) 17–24.

[59] O. Allix, P. LadevÃľze, A. Corigliano, Damage analysis of interlaminar fracture specimens, Comp. Struct. 31 (1) (1995) 61–74.

[60] G. Alfano, E. Sacco, Combining interface damage and friction in a cohesive-zone model, Int. J. Num. Meth. Eng. 68 (5) (2006) 542–582.

[61] R. Serpieri, G. Alfano, Bond-slip analysis via a thermodynamically consistent interface model combining interlocking, damage and friction, Int. J. Num. Meth. Engng. 85 (2) (2011) 164–186.

[62] Y.-C. Xiao, S. Li, Z. Gao, A continuum damage mechanics model for high cycle fatigue, International Journal of Fatigue 20 (7) (1998) 503 – 508. doi:https://doi.org/10.1016/S0142-1123(98)00005-X.
URL http://www.sciencedirect.com/science/article/pii/S014211239800005X

[63] Q. Deng, C. G. Li, S. L. Wang, H. Tang, H. Zheng, A new method to the treatment of corners in the bem, Engineering Analysis with Boundary Elements 37 (1) (2013) 182 – 186. doi:https://doi.org/10.1016/j.enganabound.2012.03.017.
URL http://www.sciencedirect.com/science/article/pii/S0955799712001439

[64] J. R. Rice, Mathematical analysis in the mechanics of fracture, Fracture: an advanced treatise 2 (1968) 191–311.

[65] V. Tomar, J. Zhai, M. Zhou, Bounds for element size in a variable stiffness cohesive finite element model, International journal for numerical methods in engineering 61 (11) (2004) 1894–1920.

[66] I. Benedetti, M. Aliabadi, A three-dimensional grain boundary formulation for microstructural modeling of polycrystalline materials, Computational Materials Science 67 (2013) 249 – 260. doi:http://dx.doi.org/10.1016/j.commatsci.2012.08.006.
URL //www.sciencedirect.com/science/article/pii/S0927025612004958

[67] V. Gulizzi, A. Milazzo, I. Benedetti, Fundamental solutions for general anisotropic multi-field materials based on spherical harmonics expansions, International Journal of Solids and Structures 100 (2016) 169–186. doi:10.1016/j.ijsolstr.2016.08.014.

[68] Y. Liu, Fast multipole boundary element method: theory and applications in engineering, Cambridge university press, 2009.

[69] M. Bebendorf, Hierarchical matrices: a means to efficiently solve elliptic boundary value problems, Vol. 63, Springer Science & Business Media, 2008.

[70] I. Benedetti, M. Aliabadi, G. Davì, A fast 3d dual boundary element method based on hierarchical matrices, International Journal of Solids and Structures 45 (7) (2008) 2355 – 2376.

doi:http://dx.doi.org/10.1016/j.ijsolstr.2007.11.018.
URL //www.sciencedirect.com/science/article/pii/S0020768307005008

[71] I. Benedetti, A. Milazzo, M. H. Aliabadi, A fast dual boundary element method for 3d anisotropic crack problems, International Journal for Numerical Methods in Engineering 80 (10) (2009) 1356–1378. doi:10.1002/nme.2666.
URL http://dx.doi.org/10.1002/nme.2666

[72] T. Buchheit, B. Boyce, G. Wellman, The role of microstructure in mems deformation and failure, in: Proc. IMECE, 2002, pp. 559–566.

[73] W. Sharpe, J. Bagdahn, Fatigue testing of polysilicon – a review, Mechanics of Materials 36 (1) (2004) 3 – 11, fatigue of Advanced Materials. doi:https://doi.org/10.1016/S0167-6636(03)00027-9.
URL http://www.sciencedirect.com/science/article/pii/S0167663603000279

[74] V. L. Huy, J. Gaspar, O. Paul, S. Kamiya, Statistical characterization of fatigue lifetime of polysilicon thin films, Sensors and Actuators A: Physical 179 (2012) 251 – 262. doi:https://doi.org/10.1016/j.sna.2012.03.011.
URL http://www.sciencedirect.com/science/article/pii/S0924424712001756

[75] J. Bagdahn, W. N. Sharpe, Fatigue of polycrystalline silicon under long-term cyclic loading, Sensors and Actuators A: Physical 103 (1) (2003) 9 – 15. doi:https://doi.org/10.1016/S0924-4247(02)00328-X.
URL http://www.sciencedirect.com/science/article/pii/S092442470200328X

[76] T. L. Anderson, Fracture mechanics: fundamentals and applications, CRC press, 2017.

[77] H. Kahn, N. Tayebi, R. Ballarini, R. Mullen, A. Heuer, Fracture toughness of polysilicon mems devices, Sensors and Actuators A: Physical 82 (1) (2000) 274 – 280. doi:https://doi.org/10.1016/S0924-4247(99)00366-0.
URL http://www.sciencedirect.com/science/article/pii/S0924424799003660

[78] Z. Hashin, S. Shtrikman, A variational approach to the theory of the elastic behaviour of polycrystals, Journal of the Mechanics and Physics of Solids 10 (4) (1962) 343–352.

[79] A. Manonukul, F. P. E. Dunne, High– and low–cycle fatigue crack initiation using polycrystal plasticity, Proceedings of the Royal Society of London A: Mathematical, Physical and Engineering Sciences 460 (2047) (2004) 1881–1903. arXiv:http://rspa.royalsocietypublishing.org/content/460/2047/1881.full.pdf, doi:10.1098/rspa.2003.1258.
URL http://rspa.royalsocietypublishing.org/content/460/2047/1881

[80] I. Benedetti, V. Gulizzi, V. Mallardo, A grain boundary formulation for crystal plasticity, International Journal of Plasticity 83 (2016) 202 – 224. doi:http://dx.doi.org/10.1016/j.ijplas.2016.04.010.
URL //www.sciencedirect.com/science/article/pii/S0749641916300596

[81] X. Wu, Y. Katada, Strain-rate dependence of low cycle fatigue behavior in a simulated bwr environment, Corrosion Science 47 (6) (2005) 1415–1428. doi:https://doi.org/10.1016/j.corsci.2004.07.037.
URL https://www.sciencedirect.com/science/article/pii/S0010938X04002410

[82] L. Beirão da Veiga, F. Brezzi, L. D. Marini, Virtual elements for linear elasticity problems, SIAM Journal on Numerical Analysis 51 (2) (2013) 794–812.

[83] M. Marino, B. Hudobivnik, P. Wriggers, Computational homogenization of polycrystalline materials with the virtual element method, Computer Methods in Applied Mechanics and Engineering 355 (2019) 349 – 372. doi:https://doi.org/10.1016/j.cma.2019.06.004.
URL http://www.sciencedirect.com/science/article/pii/S0045782519303445

[84] M. Lo Cascio, A. Milazzo, I. Benedetti, Virtual element method for computational homogenization of composite and heterogeneous materials, Composite Structures 232 (2020) 111523.

[85] M. LoCascio, M. Grifò, A. Milazzo, I. Benedetti, Computational homogenization of heterogeneous materials by a novel hybrid numerical scheme, Journal of Multiscale Modelling 11 (04) (2020) 2050008.

[86] M. Lo Cascio, A. Milazzo, I. Benedetti, A hybrid virtual–ĂŞboundary element formulation for heterogeneous materials, International Journal of Mechanical Sciences 199 (2021) 106404. doi:https://doi.org/10.1016/j.ijmecsci.2021.106404.
URL https://www.sciencedirect.com/science/article/pii/S0020740321001399

[87] I. Benedetti, M. H. Aliabadi, A fast hierarchical dual boundary element method for three-dimensional elastodynamic crack problems, International Journal for Numerical Methods in Engineering 84 (9) (2010) 1038–1067. doi:10.1002/nme.2929.
URL http://dx.doi.org/10.1002/nme.2929

[88] A. Milazzo, I. Benedetti, M. Aliabadi, Hierarchical fast bem for anisotropic time-harmonic 3-d elastodynamics, Computers & Structures 96-97 (Supplement C) (2012) 9 – 24. doi:https://doi.org/10.1016/j.compstruc.2012.01.010.
URL http://www.sciencedirect.com/science/article/pii/S0045794912000259